The influence of the Gulf Stream induced SST gradients on the U.S. East Coast winter storm of 24-25 January 2000

N. A. JACOBS*†, S. RAMAN‡, G. M. LACKMANN‡, and P. P. CHILDS JR.†

†AirDat LLC, 2400 Perimeter Park Dr., Suite 100
Morrisville, NC 27560

‡Department of Marine, Earth, and Atmospheric Sciences,
North Carolina State University, Raleigh, NC 27695-8208

February 10, 2008

Abstract

This study presents an investigation of the influence of remotely sensed high resolution sea-surface temperature (SST) and the SST gradient on the formation and evolution of the 24-25 January 2000 East Coast winter storm. A numerical model was employed for control and experimental simulations of this event. The parameters for the control and the experimental simulations were identical with the exception of the SST analysis. The source of the SST data for the control simulation was the National Centers for Environmental Prediction (NCEP) 2.5° gridded data set, while the source for the experimental simulation was a remotely sensed high resolution 1.1-km gridded data set.

The overall performance of the experimental simulation was closer to the observations than the control simulation for this major event. The most significant improvements were seen in the forecast deepening rate and track where the lowest central sea-level pressure in the experimental simulation was 7 mb lower than that in the control simulation, and the largest differences in forecast position were more than 150 km closer to the analyzed track. Reduced development of the storm in the control simulation, as compared to the experimental simulation, appears to be due to the coarse grid SST representation, which fails to capture key thermal gradient features of the Gulf Stream. The simulations suggest that the high-resolution remotely sensed SST data affect the track by changing the location of lower-tropospheric frontal boundaries through thermally-induced near-surface convergence and differential turbulent heat flux. Enhanced vortex stretching associated with the convergence along the lower frontal boundary appears to contribute to a stronger storm in the experimental simulation. The coastal front, which formed above the strong thermal gradient along the western boundary of the Gulf Stream, is much weaker in the control simulation.

1. Introduction

The rapidly intensifying coastal storms that develop along the East Coast of the U.S. during the fall, winter and spring months are widely recognized to form preferentially in this area due in part to the proximity of the Gulf Stream (GS; e.g., Sanders and Gyakum 1980; Roebber 1984). These extratropical cyclones can produce gale force winds, heavy snow, ice, and coastal storm surges with intense beach erosion, and are at times responsible for severe property damage along the Eastern Seaboard. The majority of these storms form within the coastal zone from South Carolina to Virginia. Many studies have been conducted on the GS-related air-sea interactions associated with extratropical cyclogenesis within this unique region (e.g., Bosart et al. 1972; Sanders and Gyakum 1980; Bosart 1981; Rogers and Bosart 1986; Grossman 1988; Kuo and Reed 1988; Kuo and Low-Nam 1990; Reddy and Raman 1994).

Although the role of marine boundary-layer processes during intense cyclogenesis has received considerable attention in the scientific literature (e.g., Uccellini 1990), questions remain concerning the requisite resolution of lower-boundary condition fields for the operational forecasting of coastal storms forming in this highly baroclinic environment. Operational prediction of these storms remains a challenge, as evident from the model difficulties with storms such as the January 2000 East Coast cyclone (e.g., Zhang et al. 2002; Brennan and Lackmann 2005).

Owing to the high-impact weather associated with this storm, along with the failure of operational NWP models to provide adequate guidance for this event along the Eastern

Seaboard, this case received abundant attention in the research community. Some investigations have centred on the role of initial conditions and data assimilation (e.g., Buzzia and Chessa 2002; Langland et al. 2002; Zupanski et al. 2002; Jang et al. 2003; Kleist and Morgan 2005). Other studies have examined the role of moist processes and elevated convection early in this event (e.g., Zhang et al. 2002, 2003; Brennan and Lackmann 2005; Kleist and Morgan 2005). Here, we examine the sensitivity of numerical predictions of this storm to the representation of the sea surface temperature (SST) in a numerical model.

The potential role of the lower boundary can be understood from a variety of perspectives. Following an outbreak of cold continental air over the GS, lower-tropospheric destabilization and moistening result, and a coastal frontal zone frequently forms (e.g., Austin 1941; Carson 1950). Upon the arrival of an upper-tropospheric disturbance such as a mobile upper trough, the effectiveness of vortex stretching is enhanced in the frontal zone due to the presence of pre-existing vorticity. This vortex stretching enhances cyclone spin-up, and can influence the track of the cyclone. The objective of this study is to investigate the role of the GS and the SST gradients in the development of such an East Coast extratropical cyclone using the 24-25 January 2000 storm as an example. This study tests the hypothesis that the track and intensity of the storm in the model forecasts are sensitive to the resolution and accuracy of the initial SST conditions.

2. Background

2.1. Marine thermal gradient

The southeasterly facing coastline of the Carolinas yields a favourable angle for the perpendicular offshore flow typical of the winds from a cold-air outbreak (Wayland and Raman 1989). This scenario enhances the background thermal contrast resulting from the GS in proximity to a colder land surface. Previous studies have shown that pre-storm destabilization of the lower troposphere may increase the likelihood for subsequent rapid cyclogenesis (e.g., Holt and Raman 1990; Kuo et al. 1990; Fantini 1991). Large SST gradients, perpendicular to the mid-Atlantic coast, are seen during fall, winter, and spring months because of the presence of the GS, which can have SSTs 15 to 20˚C warmer than near-coastal waters (Wayland and Raman 1989). Vukovich et al. (1991) observed that the largest values and strongest gradients of surface heat flux during a cold-air outbreak occur offshore to the north and east of Cape Hatteras, North Carolina. This is because the geographical setting allows for very little time and distance for the colder continental air mass to modify before encountering the much warmer underlying waters offshore. The strength of the baroclinity in the Marine Boundary Layer (MBL) can fluctuate with the migration of the GS relative to the coast. The degree of the MBL baroclinity is dependent on the ratio of the offshore-onshore air temperature difference to the distance of the Gulf Stream Front (GSF) from the coast.

The strong horizontal thermal gradients in this region, when combined with a cold offshore flow, can result in the rapid and intense destabilization of the MBL over the GS region thus increasing convection (Cione et al. 1998). The reduced static stability can favourably influence the deepening rate of winter cyclones (e.g., Bunker 1976; Chou et al. 1986; Reed and Albright 1986; Dirks et al. 1988; Raman and Riordan 1988; Kuo et al. 1990; Warner et al. 1990; Cione et al. 1993; Xie et al. 1999).

Cione et al. (1993) show that the pre-storm baroclinity, which includes the pre-storm GSF position, SSTs, and average coastal air temperatures, is correlated to the intensification of coastal cyclones. Results from the Cione et al. (1993) study reveal that the rate of surface cyclonic intensification is related to both the thermal structure of the continental airmass and the position of the GSF in relation to land.

The distance of the GSF from the coast can fluctuate significantly. Lateral meandering of the GSF makes these distances vary, such that at Cape Hatteras, North Carolina, offshore distance to the GSF can vary from 10 to 100 km from the coast, while offshore of Wilmington, North Carolina, the front can vary between 50 and 200 km (Cione et al. 1993). These variations are caused by the lateral or cross-shelf meandering of the GSF. Meandering of the GS, which is essentially a manifestation of the down stream propagation of topographic Rossby waves, is generated by bathymetric curvature at the site of a topographic bump or hill-like bottom feature offshore of Charleston, South Carolina located at 32°N and 79°W; also known as the Charleston "bump" (Brooks and Bane 1978; Pietrafesa et al. 1978; Rooney et al. 1978; Pietrafesa et al. 1985; Xie et al. 2007).

2.2. Boundary layer baroclinity

Although it is assumed that large scale baroclinic processes are the single most important factor in the development of cyclones (e.g., Rogers and Bosart 1986; Sanders 1986a), evidence shows that surface heat fluxes, and their horizontal gradient leading to boundary layer baroclinity, work in conjunction with the large-scale processes during the explosive growth of a marine cyclone (e.g., Kuo and Reed 1988; Holt and Raman 1990; Huang and Raman 1990; Kuo and Low-Nam 1990; Cione et al. 1993; Xie et al. 1999; Giordani and Caniaux 2001).

The influence of the GS on the overlying atmosphere is a significant factor in determining the nature of the cyclogenesis process in this region. The Atlantic Surface Cyclone Intensification Index (ASCII) is a forecast index that quantifies the strength of low-level baroclinity off the coast of the Carolinas during a cold-air outbreak. ASCII is based on the gradient between the coldest 24-h average air temperature at the coast during a cold-air outbreak and the satellite-derived SST and position of the GSF. The subsequent pre-storm baroclinic index (PSBI) indicates the potential for rapid cyclogenesis, provided an upper-tropospheric disturbance is approaching the area, and can explain as much as 31% of the storm deepening rate variance (Cione et al. 1998). Jacobs et al. (2005) found that as much as 74% of the variance in deepening rate can be explained by the surface-level thermal gradient when the absolute vorticity of the upper-tropospheric disturbance is used to categorize extratropical cyclone events.

3. 24-25 January 2000 case

Four days prior to the 24 January 2000 storm, an area of low pressure developed along the Carolina coast and tracked northeast off the mid-Atlantic U.S. A high pressure system extended southeastward behind this first coastal low, and northwesterly winds advected cold air across the coast of the Carolinas and over the GS. The 24-h air temperature observations beginning 1200 UTC 20 January decreased as much as 15°C in the coastal region between Wilmington, North Carolina (station KILM) and Morehead City, North Carolina (station CLKN7), which is consistent with the National Centers for Environmental Prediction (NCEP) North American Regional Reanalysis (NARR). This

offshore flow remained in place for more than 48 h, and was followed by the development of a coastal front over the western edge of the GS as shown in Fig. 1a. It should be noted that NARR SSTs are derived from 1-degree by 1-degree Reynolds SST data, which is a weekly average (Reynolds et al. 2002; Mesinger et al. 2006). The primary intent for the inclusion of 2-m temperature reanalysis in Fig. 1 is for land-based comparison and not over the open ocean. The observation-based verification over the ocean is discussed below.

The surface low associated with the 24 January 2000 cyclone formed in the northern Gulf of Mexico, and began to track along this stationary coastal front northeast of Florida (Fig. 1b), and downstream from an upper-level trough. As it moved over the GS from Charleston, South Carolina to Cape Hatteras, North Carolina, the pressure dropped at a rate in excess of 1.3 mb h^{-1} (cf. Fig. 1b, Fig. 1c, and Fig. 1d). The closed circulation was located east of South Carolina at 0000 UTC on 25 January (Fig. 1c), and moved northeast, parallel to the coast, following a frontal boundary that established along the temperature gradient formed by the western boundary of the GS. The surface low continued to move north, and was located east of New England by 0000 UTC 26 January. The winter storm brought heavy snowfall from the Carolinas through the New England region. Record snow amounts fell across central North Carolina with the Raleigh-Durham (RDU) airport reporting a snowfall accumulation of 20.3 in (50.8 cm). (NCDC 2000a).

Prior to the explosive development, the NCEP Eta Model's 0000 UTC 24 January run failed to accurately predict not only the track, but the deepening rate and the precipitation amount for the event (e.g., Buizza and Chessa 2002; Zhang et al. 2002). Most operational forecasts exhibited an eastward bias in storm track, and forecasted less than 5 mm liquid equivalent precipitation for the RDU area. Additional studies have been conducted on this case in an attempt to understand the sources of forecast error (e.g., Tracton and Du 2001; Langland et al. 2002; Zupanski et al. 2002; Jang et al. 2003; Brennan and Lackmann 2005). During this event, the GSF was less than 50 km off the shoreline of southeast North Carolina. As a result, the pre-storm baroclinic index was estimated to be greater than 2°C 10^{-1} km^{-1} suggesting that rapid cyclogenesis was likely.

4. Model Description

The control and experimental simulations (denoted CNTL and EXP hereafter) were conducted using the NCAR/PSU MM5 version 3.6 (e.g., Dudhia 1993; Grell et al. 1994; Haagenson et al. 1994). A single 10-km domain was initialized at 0000 UTC 24 January 2000 with the NCEP operational analysis from the Eta-212 (40-km) grid. In both simulations, the domain has 38 vertical σ-levels between 1000 hPa and 100 hPa with 18 of the σ-levels below 850 hPa in the region over the ocean. The model forecast was run for 48 hours (0000 UTC 26 January).

The Kain-Fritsch cumulus parameterization scheme was used to account for sub-grid scale convection (Kain 2004), and the Eta Mellor-Yamada (Eta M-Y) planetary boundary layer (PBL) flux parameterization scheme was selected for the mixed layer (Mellor and Yamada 1982; Betts et al. 1997). The advanced cloud radiation scheme was used for radiation parameterization, and the simple ice scheme was used for cloud physics. This scheme uses explicit equations for cloud water, rain water, ice and water vapour. There is no supercooled water and immediate melting of snow below the freezing level. The NOAH Land Surface Model (LSM), in conjunction with weekly snow cover analysis from the NCEP reanalysis, was chosen for both simulations (Kalnay et al. 1996; Ek et al.

2003). However, previous testing of various LSMs for this case revealed no significant differences. Sensitivity studies suggest that snow cover and the lack of vegetation during the winter months reduce the influence of the LSM on the atmospheric surface layer (Chen and Dudhia 2001).

The EXP was identical to CNTL in every respect except for the SST analysis. Unlike the NCEP Global Data Assimilation System (GDAS) 2.5° gridded SST data from the CNTL shown in Fig. 2a, high resolution remotely sensed SST data were prescribed for the EXP (Fig. 2b). To create the experimental SST field seen in Fig. 2b, the SST grid file used to initialize the CNTL (Fig. 2a), was overwritten with the Eta-212 SST, and the new 1.1-km high resolution remotely sensed data matrices were quilted over corresponding latitude and longitude grid coordinates. The 1.1-km SST data were derived from digital images acquired by the Advanced Very High Resolution Radiometer (AVHRR) carried onboard the NOAA-12 and NOAA-14 polar orbiting satellites, and obtained through NOAA's CoastWatch program (Li et al. 2002). The first step in the SST preprocessing was to obtain single pass 1.1-km resolution data sets by analyzing imagery preceding storm development with as little cloud cover as possible. The chosen imagery was from 22 January 2000, less than 48 h prior to the start of the simulation. This was early enough to reveal the dominant features of the GS, yet preceded the increase in cloud cover. This imagery was less than 10% corrupted with cloud cover interference. Preprocessing code developed at the State Climate Office of North Carolina was used to interpolate the remaining SST grid values where the cloud interference occurred.

Once the cloud-free SST data set was constructed, it was mapped over the 10-km regridded analysis generated with the Eta-212 SST data set. The final SST file used to initialize the EXP is shown in Fig. 2b. This mapping process involved multiple 512 x 512 matrices, the eastern boundaries of which are distinguishable in Figure 2b. The mapping covered the zones extending beyond the eastern and northern edges of the GS to fully encompass the GSF features. Ship and buoy observations were compared against the imagery in the data set to validate the SST off the southeast coast of North Carolina. The SST observations for 23 January 2000 are shown in Fig. 3. Large SST values of 24°C east of Cape Hatteras, North Carolina and 23°C southeast of Cape Hatteras, North Carolina were observed by ships and buoys, and verify the presence of the warm-core filament seen in the imagery (Fig. 2b and Fig. 3).

It is the region of maximum SST gradient near the western edge of the GS where the SST changes from 282 to 297 K (i.e., mainly along the coast from 33°N to 37°N; Fig. 2b) that appears to be associated with the dominate surface forcing and storm intensification during this event. The discontinuities seen in Fig. 2b along the southern and eastern boundaries are numerically insignificant based on their magnitude and location with respect to the developing storm. These SST variations along the southern and eastern boundaries are minimal (1-3°C) and do not produce significant boundary layer baroclinity. On the other hand, the coastal SST gradients are quite significant, exceeding 16°C over a similar distance. It would have been desirable to have the entire domain covered by the remotely sensed high resolution data; however, at the time of the January 2000 storm, only the two grids employed here were available.

5. Results

The tracks and sea-level pressures of the EXP (dashed), CNTL (dotted), and observations (solid) are shown in Fig. 4. Corresponding positions of the simulated storms are marked with the respective times. The sea-level pressures at those times are listed in a text box within Fig. 4. Sea-level pressure time series for the CNTL, EXP, and observed minimum central pressure are shown in Fig. 5. There are discrepancies between the NARR sea-level pressure, generated on the NCEP 221 grid (32-km), and the observed lowest central sea-level pressures of the cyclone (cf. Fig. 1, Fig. 4, and Fig. 5). For this study, the observations presented in Figs. 4 and 5 are taken as the truth. It should be noted that during the first 12 h after 0000 UTC 24 January, prior to a dominant cyclonic feature, the minimum central low pressure at the surface level occurred at different locations along the coastal front. Although there was approximately 150 km difference in horizontal position prior to 2100 UTC 24 January between the simulations and the observed position, there was no significant variation in minimum central sea-level pressure between the simulations until 0600 UTC 25 January (30 h, Fig. 5). This is likely due to less accurate Eta-212 analysis fields during model initialization, the low density of offshore observations, and the inability to ascertain the exact position of the low-level centre due to multiple areas of equal low pressure. At 0600 UTC 25 January, the motion, or speed, of the centre of the low in the EXP was faster and closer to the observed position.

Between 0600 and 0900 UTC 25 January, the sea-level pressure in the EXP decreases at a rate greater than that of the CNTL, and by 0900 UTC 25 January, the sea-level pressure of the EXP is 2 mb lower. At the time this pressure drop in the EXP begins, the centre of the low pressure system is crossing the warm-core filament east of Cape Hatteras, North Carolina, located at 35°N, 74.5°W (cf. Fig. 3 (circle) and Fig. 5). However, in the CNTL, the low is not accelerating at the same rate, nor does it experience the abrupt pressure decrease by 0900 UTC 25 January. The lateral position of the storm in the EXP is slightly to the west of that in the CNTL, and closer to the observed track. The closer proximity of the EXP is primarily a function of the faster progression, as the latitudinal differences between the EXP and the observed position are much less than the CNTL. When the simulated storm is passing east of Cape Hatteras, North Carolina from 0900 UTC to 1600 UTC 25 January, the longitudinal position of the centre of circulation in the CNTL is about 80 km east of the EXP. The sea-level pressure for the EXP at 1600 UTC 25 January is 982 mb. This is 6 mb lower than that in the CNTL, and 4 mb higher than the analyzed pressure of 978 mb.

The inability of the EXP to match the observations can likely be attributed to sources such as the incipient precipitation-induced lower-tropospheric cyclonic PV anomaly, which contributed to the deepening of the height field beginning around 1500 UTC 24 January (Brennan and Lackmann 2005), and is consistent with findings presented here (Fig. 5), as well as forecast error growth with downstream propagation of initial perturbations (Zhang 2005). The cyclone in the EXP is within approximately 100 km of the observed position of the storm by 1600 UTC 25 January; however, the CNTL begins to lag the forward speed of both the EXP and the observed storm.

Beyond 37°N, the CNTL cyclone veers further east. During this time, the cyclone in the EXP follows a track much closer to that of the observed storm. The largest difference in surface pressure between the simulations also occurs at this point (42 h, or 1800 UTC 25 January), with the EXP 7 mb lower than the CNTL (Fig. 5). As the storm in

the EXP moves off the region of high resolution SST (beyond 44 h), not only do the sea-level pressure differences between the two simulations decrease, but the pressures rise in both simulations as the occluded storm begins to weaken. By 2300 UTC 25 January, the central low pressure in the CNTL is more than 150 km southeast of that in the EXP, which is only 50 km east of the observed low, and following a similar track.

Plots of 10-m wind vectors and 2-m air temperatures are shown in Fig. 6, which is valid 1200 UTC 24 January. A line of convergence along a frontal boundary extending off the northeast quadrant of the central area of low pressure (arrow), or about 200 km east-southeast of Charleston, South Carolina is seen in both simulations. At this time, the differences in 10-m wind vectors are negligible. However, a noticeable difference in the 2-m air temperatures can be seen in the region circled, where the EXP, shown in Fig. 6b, has values averaging 3°C higher than the CNTL (Fig. 6a). Since the convergence is aligned with the 293 K isotherm in both simulations, there is minimal difference in the position of the coastal front at this time. This is likely due to the fact that it is just 12 h into both simulations, which were initialized with the same atmospheric data.

The differences in the 10-m wind and 2-m temperature fields, valid 0000 UTC 25 January, between the CNTL (Fig. 7a), and the EXP (Fig. 7b) continue to evolve as the coastal front becomes better established. The simulated 2-m air temperature in the EXP continues to exceed that in the control by about 4°C in the same location (circled). However, this region (circled) has extended farther to the south in the EXP (Fig. 7b) where values are actually 2-3°C cooler than in the CNTL. The previous region of convergence shown in Fig. 6, beginning at 33°N, 75°W and extending northeast, is still seen in the CNTL of Fig. 7a (arrow), but has shifted southeast in the EXP (Fig. 7b, arrow "A"). The surface circulation is still evident in both simulations, as well as a new area of convergence (arrow "B") along a rapidly forming coastal front located along the 291 K isotherm in the EXP (Fig. 7b). This coastal front, which is more pronounced in the EXP, spans the entire length of the western boundary of the GS.

The 10-m convergence (shaded, 10^{-4} s^{-1}) and the σ-based level (approximately 700 hPa) of maximum divergence (dashed contours, 10^{-4} s^{-1}) valid 0000 UTC 25 January, are shown in Fig. 8. Values greater than 4×10^{-4} s^{-1} are seen extending off the northeast quadrant of the low pressure system in both simulations. The horizontal extent of convergence larger than 1×10^{-4} s^{-1} in the CNTL (Fig. 8a) is much shorter in length, and less defined as compared to the EXP (Fig. 8b).

The CNTL has maximum 10-m convergence values reaching 5×10^{-4} s^{-1} in the region of 32°N, 77°W near the vicinity of the low-level circulation. The 10-m convergence for the EXP exhibits maximum values of 7×10^{-4} s^{-1} parallel to the coastline for a greater distance along the thermal gradient of the GSF from the surface low pressure to 38°N, 71.5°W (Fig. 8b). This region, which corresponds to the location of the coastal front, is consistent with the 10-m wind field shown in Fig. 7b. The 10-m convergence in the region of the low-level circulation located at 32°N, 77°W of the EXP shares similar position and magnitude with the CNTL. However, the maximum value of larger than 5×10^{-4} s^{-1} in the EXP, located 320 km north of the low-level circulation (Fig. 8b), corresponds to a warm-core GS filament seen in Fig. 2b and Fig. 3 (circle).

The 700-hPa divergence (dashed contours, 10^{-4} s^{-1}) valid 0000 UTC 25 January (Fig. 8) aligns with the surface convergence, and the magnitude of this divergence appears to be related to the magnitude of the surface convergence (cf. Fig. 8a, Fig. 8b). This is

likely in response to the SST-related enhanced surface dynamics simulated in the EXP case.

A cross section valid at 0000 UTC 25 January (Fig. 9) is taken from 79°W to 72°W along 34.4°N across the GSF meander and through the developing coastal front (cf. Fig. 7, Fig. 9). The alternate perspective suggests that the increased 700-hPa divergence (dashed contours, 10^{-4} s^{-1}), as well as the low-level convergence (solid contours, 10^{-4} s^{-1}), seen in the EXP (Fig. 9b) is associated with the upward motion, represented as vertical velocity contours (Fig. 9b, shaded, m s^{-1}). At this time (0000 UTC 25 January) and latitude (34.4°N), the frontogenesis is occurring in nearly the same longitudinal location; however, it is significantly more pronounced in the EXP case (cf. Fig. 9a, Fig. 9b).

The 10-m convergence (shaded, 10^{-4} s^{-1}) and 700-hPa divergence (dashed contours, 10^{-4} s^{-1}) valid 1200 UTC 25 January, are shown in Fig. 10 along with sea-level pressure. Both the CNTL and EXP share a similar region of surface convergence in the vicinity of 38°N, 71.5°W, albeit different magnitudes (cf. Fig. 10a, Fig. 10b). However, the surface convergence closer to the centre of circulation in both simulations is quite different. The EXP (Fig. 10b) produces a more defined and intense convergence zone just north of the centre of the surface low pressure, which is also slightly north of the centre of the low pressure seen in the CNTL (Fig. 10a). As expected, the majority of the 700-hPa divergence continues to be associated with the surface convergence in both simulations; however, in the CNTL, the centre of the surface low pressure appears to be lagging the leading zone of maximum divergence (Fig. 10a).

To provide a more consistent comparison, the corresponding cross sections, valid 1200 UTC 25 January, have been made diagonally through the active surface convergence area of both simulations. Since the region of the most active surface convergence is located in different locations for each simulation, the cross sections in Fig. 11 span 35.25°N, 75°W ("A") to 38°N, 70°W ("B") for the CNTL and 36.25°N, 75°W ("A") to 39°N, 70°W ("B") for the EXP, as drawn in Fig. 10. At this point, significant differences in the position (> 100 km) of frontogenesis between the CNTL (Fig. 11a) and the EXP (Fig. 11b) are evident. The magnitude of the low-level convergence (solid contours, 10^{-4} s^{-1}) and the mid-level divergence (dashed contours, 10^{-4} s^{-1}) in the EXP (Fig. 11b, 71.3°W) is noticeably larger than the CNTL (Fig. 11a, 71.3°W), and the region of upward motion appears to be more focused in the EXP. In the CNTL, the low-level convergence is broader and less defined. The vertical velocity associated with the more enhanced dynamics of the EXP exceeds 1.2 m s^{-1} around 800 hPa. The magnitude of the divergence associated with this feature in the EXP ($> 8 \times 10^{-4}$ s^{-1}) is almost twice that of the CNTL.

Additionally, enhanced upward motion is also seen to the west of the surface low pressure in the EXP, and extends well above 700 hPa (Fig. 11b, 72.5°W to 73.5°W). The CNTL also exhibits a faint zone of upward motion in a similar location, which is implied by the low-level convergence and 750-hPa divergence (Fig. 11a, 72.8°W), but the magnitude is negligible in comparison with the EXP. This suggests that SST-induced surface forcing has the ability to generate a dynamic response in the middle and upper-troposphere with adequate model spin-up time.

Surface sensible heat flux in W m^{-2} valid 0000 UTC 25 January for the CNTL is shown in Fig. 12a. There is a large region with heat flux values greater than 250 W m^{-2} located off the southeast coast of the Carolinas (Fig. 12a, "A"). The sensible heat flux values in the EXP, shown in Fig. 12b, valid 0000 UTC 25 January, exceed that of the CNTL (Fig. 12a) located off the Carolinas (Fig. 12b, "A") extending well northeast of Cape

Hatteras, North Carolina (Fig. 12b, “B”) by more than 300 W m^{-2}. It is evident that the well defined GSF of the EXP is influencing the surface-level dynamics. Values of sensible heat flux from 300 to 400 W m^{-2} can be seen in Fig. 12b along the western GS boundary parallel to the coastline. The largest difference between the EXP and CNTL of more than 350 W m^{-2} (Fig. 12c, arrow) is located about 100 km south of Cape Hatteras, North Carolina. Sea-level pressure contours shown in Fig. 12b (particularly 1004 to 1008 mb) also align with regions of elevated sensible heat flux along the GSF due to increased winds extending northeast of Cape Hatteras, North Carolina.

By 1200 UTC 25 January (36 h after initialization), the fully developed storm is following a track northeast of Cape Hatteras, North Carolina as shown in Fig. 13. In both simulations, elevated sensible heat flux values greater than 325 W m^{-2} can be seen off South Carolina as a result of the cold dry air advecting over the warm water (Figs. 13a and 13b, "A"). The sensible heat flux values in the EXP exceed those in the CNTL by 50 to 100 W m^{-2} in the region slightly to the northeast of "A" (Fig. 13c, "B"). However, north and west of the preceding edge of the centre of circulation (Fig. 13c, "C1" and Fig. 13c, "C2") , the sensible heat flux in the EXP is 400 W m^{-2} larger than the CNTL. This is likely a result of a more defined heat flux gradient corresponding to the location of a warm-core filament, which can be seen off the Delmarva Peninsula (38.5°N, 72°W, Fig. 2b), as well as the elevated SSTs (> 22°C) within that filament.

The largest values of sensible heat flux near the centre of circulation in the EXP exceed 500 W m^{-2}; however, in the CNTL, values never exceed 200 W m^{-2} near the centre of the cyclone. This is partly because of the lack of storm development in the CNTL, probably caused by relatively lower SST values. In both simulations (Fig. 13a,b, “A”), elevated sensible heat fluxes can be seen to the southwest side of the circulation in the wake of the surface low. This is consistent with strong cold advection, but is not considered a direct factor in storm intensification (e.g., Nuss and Anthes 1987, and Kuo et al. 1990).

A ridge-trough couplet can be seen in the sea-level pressure of the CNTL at 1200 UTC 25 January near 37.5°N, 72°W (Fig. 13a and Fig. 10a). It appears to be a response to the sensible heat flux; however, it is not as developed in the EXP, which initially seems to contradict the hypothesis that the low-level mesoscale features will be better resolved in the EXP. A more thorough investigation reveals a small upper-level shortwave trough feature embedded in the flow downstream of the main upper-level trough axis, which first appears around 0600 UTC 25 January in both simulations.

In the EXP, there is low-level warm air advection surrounding the upper-level shortwave axis due to its position as it crosses the warm-core filament. The negative vorticity advection on the backside of the shortwave is overcome by the positive vorticity advection that is associated with the low-level warm air advection and convergence-induced rising motion seen in Figs. 10b and 11b. This extends the surface trough westward in the EXP, where the trailing effects of the shortwave-induced surface ridge-trough couplet can be seen in alignment with the western thermal gradient boundary of the warm-core filament. In the CNTL, which does not contain this SST feature, there is no significant low-level warm air advection to counter the subsidence-induced ridge seen in the wake of the shortwave. The evolution of the future low-level warm air sources can be seen in the 2-m temperatures and 10-m winds presented in Fig. 7.

The additional increase in surface-level wind in the EXP in this vicinity is likely a result of positive feedback caused by the high SST values of the warm-core filament, which

further reduces the low-level static stability. As a result of the elevated surface winds (discussed below), the low-level warm air advection is enhanced by greater sensible heat flux. Likewise, in the CNTL, an increase in low-level static stability likely plays a role in lower sensible heat flux by decreasing the surface-level winds (Sweet et al. 1981; Desjardins et al. 1998; Von Ahn et al. 2006).

The coastal frontogenesis, evident by 0000 UTC 25 January, is taking place along a line 32°N, 77°W to 37°N, 72°W in Fig. 14b ("A") of the EXP more so than Fig. 14a of the CNTL. The coastal front seen in the EXP (Fig. 14b) has winds 2-4 m s^{-1} larger than those in the CNTL. These are consistent with estimates based on the pressure gradient difference between the simulations, as well as the convergence contours of Fig. 8b, which are about 3 × 10^{-4} s^{-1} larger in the EXP. Values of wind speed just east of the front in Fig. 14b ("B") are 4 to 6 m s^{-1} lower than in the CNTL shown in Fig. 14a ("B"). More importantly, the transition where the winds decrease east of the front in Fig. 14b is more abrupt for the EXP. Both figures are valid 0000 UTC 25 January (24 h into the simulation), and share similar wind velocity values of 11-13 m s^{-1} (20-25 kts) over the region east of South Carolina ("C"). At a location northeast of Cape Hatteras, North Carolina, the EXP (Fig. 14b) shows a slightly larger region of winds of magnitude 16 m s^{-1} (31 kts) with a few small areas of simulated winds over 17 m s^{-1}. In addition to the regions of increased wind speed west of the coastal front, the EXP shows a region of winds with values 4 m s^{-1} (8 kts) less than that of the CNTL east of the front.

Thirty six hours into the simulation (1200 UTC 25 January), the fully developed low pressure system in the CNTL, shown in Fig. 15a, is located about 180 km due east of Cape Hatteras, North Carolina (cf. Fig. 13a). The position of the low in the EXP, shown in Fig. 15b, located at 37°N, 73°W, is about 80 km to the north-northwest of that in the CNTL (cf. Fig. 13b). In Figs. 15a and 15b, minor differences can be seen along the GS region east of Georgia (30.5°N) to southeast North Carolina ("A") with most of the wind speeds in the 10 to 12 m s^{-1} (23 kt) range. East of Cape Hatteras, North Carolina, near the coastline, both simulations share similar regions of 18-22 m s^{-1} or 35-43 kts (Figs. 15a,b, circled). However, closer to the centre of circulation, the 10-m winds in the EXP (Fig. 15b) exceeded those in the CNTL by about 4 m s^{-1} (8 kts) with maximum values approaching 50 kts. The region of greatest sensible heat flux difference located just off the southeast coast of North Carolina presented earlier in Fig. 13c (between "B" and "C1") is likely a result of the remotely sensed high resolution SST because the corresponding regions shown in Figs. 15a and 15b (circled) have wind speeds that differ less than 3-4 m s^{-1}. In the EXP (Fig. 15b, "B"), in the wake of the low behind the cold front, the winds are 4-5 m s^{-1} less than the CNTL. This region in Fig. 15b corresponds to a zone of high resolution and thus large gradients in SST, shown in Fig. 2b, east of the GS at 31.5°N, 75°W.

The low-level (950-hPa) vortex stretching (10^{-7} s^{-2}) valid 0000 UTC 25 January is shown in Fig. 16 for the CNTL (a), and the EXP (b). In both simulations, there are two adjacent swaths of elevated stretching linked to the coastal frontogenesis. In the CNTL (Fig. 16a), this region ("A") has maximum values of 3 × 10^{-7} s^{-2}, while there is a slightly weaker line ("B") about 200 km to the northwest which crosses the tip of Cape Hatteras, North Carolina. The ultimate path of the low pressure system in the CNTL was along a line between these two regions and slightly closer to the stronger swath of stretching to the east (cf. Fig. 16a, Fig. 4). In the EXP (Fig. 16b), the line of enhanced vortex stretching exhibits two linear maxima, similar to the CNTL; however, it is the western maximum (Fig. 16b,

"A") which is significantly more pronounced. This line has values exceeding 6×10^{-7} s^{-2}, which extend well past the latitude of Cape Hatteras, North Carolina. The track of the storm in the EXP (Fig. 4) did not veer from this path until after 1600 UTC 25 January.

Along the region "A" in Fig. 16b where the coastal frontogenesis in the EXP occurred, the magnitude of the vortex stretching is 4×10^{-7} s^{-2} to 6×10^{-7} s^{-2} greater than the CNTL. The increased deepening rate of the cyclone in the EXP, approximately 1.2 mb h^{-1}, is likely due to enhanced vortex stretching along the frontal boundary in this region as compared to the CNTL.

By 1200 UTC 25 January, the surface low pressure has deepened significantly and is located east of Cape Hatteras, North Carolina. The maximum values of 950-hPa vortex stretching in the CNTL (not shown) are much larger than those in the previous Fig. 16a, but still further to the east of those in the EXP. The magnitude of the stretching in the EXP exceeds that of the CNTL by more than 4×10^{-7} s^{-2} in the vicinity of the surface low pressure.

The simulated storm-total precipitation fields are shown for the CNTL (Fig. 17a) and EXP (Fig. 17b), as well as the verifying analysis, which is shown in Fig 17c. The 48-h accumulated liquid-equivalent precipitation observations (mm), which are derived from the 4-km multi-sensor precipitation analysis produced by the Environmental Modeling Center (EMC) at NCEP, are valid 0000 UTC 26 January 2000. The hourly digital precipitation radar estimates are combined with the Automated Surface Observation System (ASOS) gauge liquid precipitation observations to generate the analysis, and is consistent with verification presented in Zhang et al. (2002) and Zupanski et al. (2002). However, a more precise objective analysis of liquid-equivalent precipitation is conducted by Brennan and Lackmann (2005), which avoids ASOS-related biases when measuring frozen precipitation.

A slightly more westward track in conjunction with significantly more upward motion in the EXP increases the quantitative precipitation forecast (QPF; Fig. 17b). An inherent result of the overall enhanced QPF in the EXP is an increase in the magnitude of precipitation along the western edge of the storm track. This results in an increase of 10 to 20 mm of liquid-equivalent precipitation in eastern North Carolina. Despite this increase, the EXP fell far short of capturing the largest areas of precipitation that were observed along the border between North and South Carolina, as well as further west in North Carolina (Fig. 17c).

The study conducted by Brennan and Lackmann (2005) found that middle-tropospheric latent heat release from an initial band of precipitation aided in the formation of a more easterly low-level jet by enhancing a low-level diabatic potential vorticity maximum on the coast of South Carolina. The additional moisture transport from this low-level jet was found to enhance the westward extent of the precipitation field over North Carolina. The remarkably large amount of precipitation that was recorded for this event over North Carolina was likely some combination of the PV-induced low-level jet advecting the SST-enhanced low-level heat and moisture from the GS.

6. Conclusions

The main purpose of this study was to investigate the role of the GS in the development of U.S. East Coast extratropical cyclones using the 24-25 January 2000 East Coast storm. A specific objective was also to test the hypothesis that the track and intensity of the storm in the model forecasts is sensitive to the resolution of the initial SST

conditions, especially the location of the GS.

A comparison based on SST grid resolution was performed using MM5 to simulate the 24-25 January 2000 case. The parameters for the CNTL and EXP were identical, with the exception of the SST input data set. The SST data for the initialization of the CNTL were derived from the NCEP 2.5° data, and the initialization fields for the EXP were derived from remotely sensed high resolution 1.1-km SST data quilted over the Eta-212 analysis.

In this study, the SST initialization data was the only difference between the two simulations. This suggests that the frontogenetic diabatic forcing is sensitive to the magnitude and position of SST gradient. The findings presented here are consistent with those of Giordani and Caniaux (2001), who use an extension of the Hoskins et al. (1978) *w* equation (Giordani and Planton 2000) to diagnose the sources of vertical velocity, and analyze the sensitivity of *w* forcings to the surface buoyancy flux.

The overall track and intensity of the EXP (with remotely sensed high resolution SST) were closer to the observations than the CNTL. In the CNTL, reduced development of the storm may be due to geographically-coarse and temporally-averaged SST representation. The poor forecast in track position in the CNTL may be linked to the weakly defined GSF. In the EXP, the surface low tracked farther west along the more accurately represented GSF. This track is apparently the result of the surface low pressure following a zone of preexisting vorticity along the coastal front.

Large areas of convergence develop above the GSF in the EXP. The areas of convergence further offshore, as well as the minor divergent patterns along the coast, are seen in both simulations. This suggests that the greatest effect in low-level convergence occurred over the region where the resolution of the SST data was better represented.

In both simulations, the majority of the coastal region had wind speeds that differed by less than 10 kts. This suggests that the large values of sensible heat flux seen in the EXP were more a factor of the high resolution SST data than the differences in wind speeds. High resolution remotely sensed SST data revealed a more sharply defined GSF, as well as two warm-core surface filaments with SST values 5-7°C greater than that of the SST data in the CNTL. Thus, it is likely that the surface-level convection of the EXP is driven by the increased resolution of the western boundary SSTs along the GS.

In the EXP, the enhanced vertical velocity along the GSF is associated with greater surface-level convergence and frontogenesis, while the reduction in low-level static stability is a function of the increased heat flux. This convergence is the major difference in the simulations, as well as a sign that the high resolution SST data did affect the track by changing the strength and location of the frontal boundaries. Stronger near-surface vorticity is simulated in the EXP relative to the CNTL in the vicinity of the coastal front extending northeast from the low pressure centre. This coastal front, which formed above the tight marine thermal gradient of the GSF, is not seen in the CNTL. Enhanced effectiveness of vortex stretching associated with the convergence along this frontal boundary might be the reason for a stronger storm in the EXP.

This study addresses the first of three possible questions outlined by Giordani and Caniaux (2001) regarding cyclogenetic response to SST conditions by altering the magnitude of the SST gradient through increased SST data resolution.

The broader significance of this work for operational NWP indicates the need for greater emphasis to be placed on increasing the spatial and temporal resolution of SST data.

The higher spatial resolution of the SST data will enable operational models to more accurately represent the air-sea fluxes, while higher temporal resolution will enable guidance to capture the location and propagation of GSF-related features.

Acknowledgments: The authors are very grateful for the computer support provided by Robert Gilliam (US EPA). We would like to thank Dr. Fuqing Zhang (Texas A&M Univ.) for providing the archived Eta-212 GRIB files. We would also like to thank Jonathan Blaes and Kermit Keeter (NWS Raleigh, North Carolina) for their valuable suggestions. This work was supported by the Atmospheric Sciences Division, National Science Foundation under the grant ATM-0342691. The authors would like to thank both of the anonymous reviewers for their comments and suggestions to improve the manuscript.

References

Austin, J. M., 1941, Favorable conditions for cyclogenesis near the Atlantic coast. *Bulletin of the American Meteorological Society*, **22**, 270- 272.

Betts, A. K., Chen, F., Mitchell, K. E., and Janjic, Z., 1997, Assessment of the land surface and boundary layer models in two operational versions of the NCEP Eta model using FIFE data. *Monthly Weather Review,* **125**, 2896-2916.

Bosart, L.F., 1981: The Presidents' Day snowstorm of 18-19 February 1979; A synoptic scale event. *Monthly Weather Review*, **109**, 1542-1566.

Bosart, L.F., Vaudo, C. J., and Helsdon, Jr., H. J., 1972, Coastal Frontgenesis. *Journal of Applied Meteorology*, **11**, 1236-1258.

Brennan, M. J., and Lackmann, G. M., 2005, The influence of incipient latent heat release on the precipitation distribution of the 24-25 January 2000 U.S. East Coast cyclone. *Monthly Weather Review,* **133**, 1913-1937.

Brooks, D.A., and Bane, J. M., 1978, Gulf Stream deflection by a bottom feature off of Charleston, South Carolina. *Science*, **201**, 1225-1226.

Bunker, A.F., 1976, Computations of surface energy flux and annual air-sea interaction cycles of the North Atlantic Ocean., *Monthly Weather Review*, **104**, 1122-1140.

Buizza, R. and Chessa, P., 2002, Prediction of the U.S. Storm of 24-26 January 2000 with the ECMWF Ensemble Prediction System. *Monthly Weather Review*, **130**, 1531-1551.

Carson, R. B., 1950, The Gulf Stream front: cause of stratus on the lower Atlantic coast. *Monthly Weather Review*, **78**, 91- 101.

Chen, F., and Dudhia, J., 2001, Coupling an advanced land surface hydrology model with the Penn State/NCAR MM5 modeling system. Part 1: Model description and implementation. *Monthly Weather Review,* **129**, 569-586.

Chou, S. H., Atlas, D., and Yeh, E. N., 1986, Turbulence in a convective marine atmospheric boundary layer. *Journal of Atmospheric Science*, **43**, 547-564.

Cione, J. J., Raman, S., and Pietrafesa, L. J., 1993, The effect of Gulf Stream-induced baroclinicity on the U.S. East Coast winter cyclones. *Monthly Weather Review*, **121**, 421-430.

Cione, J. J., Raman, S., Neuherz, R. A., Pietrafesa, L. J., Keeter, K., and Li, X., 1998, The Use of Pre-storm Boundary Layer Baroclinicity in Determining and Implementing the Atlantic Surface Cyclone Intensification Index. *Boundary-Layer Meteorology*, **89**, 211-224.

Desjardins, S., Benoit, R., and Swail, V., 1998, The influence of mesoscale features of the sea surface temperature distribution on marine boundary layer winds off the Scotian Shelf during the Superstorm of March 1993. *Monthly Weather Review,* **126,** 2793–2808.

Dudhia, J., 1993, A nonhydrostatic version of the Penn State / NCAR mesoscale model: Validation tests and simulation of an Atlantic cyclone and cold front. *Monthly Weather Review*, **121**,1493-1513.

Ek, M. B., Mitchell, K. E., Lin, Y., Rogers, E., Grunmann, P., Koren, V., Gayno, G., and Tarpley, J. D., 2003, Implementation of Noah land-surface model advances in the NCEP operational mesoscale Eta model, *Journal of Geophysical Research*, **108**, D22, doi:10.1029/2002JD003296.

Fantini, M., 1991, The Influence of Heat and Moisture Fluxes from the Ocean on the Development of Baroclinic Waves, *Journal of Atmospheric Science,* **47**, 840-855.

Giordani, H., and Planton, S., 2000, Modeling and analysis of ageostrophic circulation over the Azores Oceanic Front during the SEMAPHORE experiment. *Monthly Weather Review*, **128**, 2270–2287.

Giordani, H., and Caniaux, G., 2001, Sensitivity of cyclogenesis to sea surface temperature in the Northwestern Atlantic. *Monthly Weather Review*, **129**, 1273–1295.

Grell, G. A., Dudhia, J., and Stauffer, D. R., June 1994, A Description of the Fifth-Generation Penn State/NCAR Mesoscale Model (MM5), Tech. Rep. NCAR/TN-398+STR, National Center for Atmospheric Research, Boulder, Colorado.

Grossman, R. L., 1988, Boundary layer warming by condensation: Air-sea interaction during an extreme cold air outbreak for the eastern coast of the United States, Seventh Conference on Oceanic-Atmospheric Interaction. American Meteorological Society, 31 January- 5 February, 1988.

Haagenson, P. L., Dudhia, J., Grell, G. A., and Stauer, D. A., 1994, The Penn State / NCAR mesoscale model (MM5) source code documentation. NCAR Technical Note, NCAR/TN-392+STR, 200 pp.

Holt, T., and Raman, S., 1990, Marine boundary-layer structure and circulation in the region of offshore re-development of a cyclone during GALE. *Monthly Weather Review*, **118**, 392-410.

Hoskins, B. J., Draghici, I., and Davies, H. C., 1978, A new look at the *w*-equation, *Quarterly Journal of the Royal Meteorological Society*, **104**, 31–38.

Huang, C. Y., and Raman, S., 1990, Numerical simulation of cold air advection over the Appalachian mountains and the Gulf Stream. *Monthly Weather Review*, **118**, 343-361.

Jacobs, N. A., Lackmann, G. M., and Raman, S., 2005, The combined effects of Gulf Stream–induced baroclinicity and upper-level vorticity on U.S. East Coast extratropical cyclogenesis. *Monthly Weather Review*, **133**, 2494–2501.

Jang, K.-I., Zou, X., De Pondeca, M. S. F. V., Shapiro, M., Davis, C., and Krueger, A., 2003, Incorporating TOMS Ozone Measurements into the Prediction of the Washington, D.C.,Winter Storm during 24–25 January 2000. *Journal of Applied Meteorology*, **42**, 797–812.

Kain, J. S., 2004, The Kain-Fritsch Convective Parameterization: An Update. *Journal of Applied Meteorology*, Vol **43**, No 1, pp170-181.

Kalnay, E., Kanamitsu, M., Kistler, R., Collins, W., Deaven, D., Gandin, L., Iredell, M., Saha, S., White, G., Woollen, J., Zhu, Y., Chelliah, M., Ebisuzaki, W., Higgins, W., Janowiak, J., Mo, K. C., Ropelewski, C., Wang, J., Leetmaa, A., Reynolds, R., Jenne, R., and Joseph, D., 1996, The NCEP/NCAR 40-Year Reanalysis Project. *Bulletin of the American Meteorological Society*, 1996, **77**,437-431.

Kleist, D. T., and Morgan, M. C., 2005, Application of adjoint-derived forecast sensitivities to the 24–25 January 2000 U.S. East Coast snowstorm. *Monthly Weather Review*, **133**, 3148–3175.

Kuo, Y. H., and Reed, R. J., 1988, Numerical Simulation of an Explosively Deepening Cyclone in the Eastern Pacific. *Monthly Weather Review*, **116**, 2081-2105.

Kuo, Y. H., and Low-Nam, S., 1990, Prediction of Nine Explosive Cyclones over the Western Atlantic Ocean with a Regional Model. *Monthly Weather Review*, **118**, 3-25

Kuo, Y. H., Reed, R. J., and Low-Nam, S., 1990, Effects of surface energy fluxes during the early development and rapid intensification stages of seven explosive cyclones in the Western Atlantic. *Monthly Weather Review*, **119**, 457-476.

Langland, R. H., Shapiro, M. A., and Gelaro, R., 2002, Initial condition sensitivity and error growth in the forecast of the 25 January 2000 East Coast snowstorm. *Monthly Weather Review*, **130**, 957-974.

Li, X., Pichel, W., Clemente-Colon, P., Krasnopolsky, V., and Sapper, J., 2002, Validation of coastal sea and lake surface temperature measurements derived from NOAA/AVHRR data, *International Journal of Remote Sensing*, **22**, 1285-1303.

Mellor, G. L., and Yamada, T., 1982, Development of a turbulence closure model for geophysical fluid problems. *Reviews of Geophysics and Space Physics,* **20,** 851–875.

Mesinger, F., DiMego, G., Kalnay, E., Mitchell, K., Shafran, P. C., et al., 2006, North American Regional Reanalysis. *Bulletin of the American Meteorological Society*, **87**, 343–360.

NCDC, 2000a, *Storm Data*. Vol. 42, No. 1, 171 pp.

Nuss, W. A., and Anthes, R. A., 1987, A numerical investigation of low-level processes in rapid cyclogenesis. *Monthly Weather Review,* **115,** 2728-2743.

Pietrafesa, L.J., Atkinson, L. P., and Blanton, J. O., 1978, Evidence for the deflection of the Gulf Stream by the Charleston rise. *Gulfstream,* vol. IV, 9, 3-7.

Pietrafesa, L. J., Janowitz, G. S., and Whittman, J., 1985, Physical oceanographic processes in the Carolina capes. *Coastal and Estuarine Science*, **2**, 23-33.

Raman, S., and Riordan, A. J., 1988, The Genesis of Atlantic Lows Experiment: The Planetary Boundary Subprogram., *Bulletin of the American Meteorological Society*, **69**, 161-172.

Raman, S., and Reddy, N. C., 1996, Numerical simulation of a mesolow over a Gulf Stream filament. *Pure and Applied Geophysics*, **147**, 789-819.

Reddy, N. C., and Raman, S., 1994, Scales and spectra of turbulence over the Gulf Stream. *Boundary-Layer Meteorology*, **68**, 387-417.

Reed, R. J., and Albright, M. D., 1986, A case study of explosive cyclogenesis in the Eastern Pacific. *Monthly Weather Review,* **114,** 2297-2319.

Reynolds, R. W., Rayner, N. A., Smith, T. M., Stokes, D. C., and Wang, W., 2002, An improved in situ and satellite SST analysis for climate. *Journal of Climate*, **15**, 1609-1625.

Roebber, P. J., 1984, Statistical analysis and updated climatology of explosive cyclones. *Monthly Weather Review*, **112**, 1577-1589.

Rogers, E., and Bosart, L. F., 1986, An investigation of explosively deepening oceanic cyclones. *Monthly Weather Review*, **114**, 702-718.

Rooney, D. M., Janowitz, G. S., and Pietrafesa, L. J., 1978, A simple model of the deflection of the Gulf Stream by the Charleston rise. *Gulfstream,* vol.4, 11, 2-7.

Sanders, F. J., and Gyakum, J. R., 1980, Synoptic-dynamic climatology of the "bomb". *Monthly Weather Review*, **108**, 1589-1606.

Sanders, F., 1986, Explosive cyclogenesis over the west-central North Atlantic Ocean, 1981-84, I, Composite Structure and Mean Behavior, *Monthly Weather Review*, **114**, 1781-1794.

Sweet, W., Fett, R., Kerling, J., and La Violette, P., 1981, Air-Sea Interaction Effects in the Lower Troposphere Across the North Wall of the Gulf Stream. *Monthly Weather Review*, **109**, 1042–1052.

Tracton, M. S., and Du, J., 2001, Application of the NCEP/EMC short-range ensemble forecast system (SREF) to predicting extreme precipitation events. *Symposium on Precipitation Extremes: Prediction, Impacts, and Responses*, Albuqerque, New Mexico, Americal Meteorological Society, *Preprints*, 64-65.

Uccellini, L. W., 1990, Processes Contributing to the Rapid Development of Extratropical cyclones. Extratropical Cyclones, Palmen Memorial Volume, C. W. Newton and E. O. Holopainen, Eds., Americal Meteorological Society, 81-105.

Von Ahn, J. M., Sienkiewicz, J. M., and Chang, P. S., 2006, Operational Impact of QuikSCAT Winds at the NOAA Ocean Prediction Center. *Weather and Forecasting*, **21**, 523–539.

Vukovich, F. M., Dunn, J. W., and Crissman, B. W., 1991, Aspects of the evolution of the marine boundary layer during cold air outbreaks off the southeast coast of the United States. *Monthly Weather Review*, **119**, 2252-2278.

Wayland, R., and Raman, S., 1989, Mean and turbulent structure of a baroclinic marine boundary-layer during the 28 January 1986 cold air outbreak (GALE86). *Boundary-Layer Meteorology*, **48**, 227-254.

Xie, L., Pietrafesa, L. J., and Raman, S., 1999, Coastal ocean-atmosphere coupling. *Coastal and Estuarine Studies*, **56**, 101-123.

Xie, L., Liu, X., Pietrafesa, L. J., 2007, Effect of bathymetric curvature on Gulf Stream instability in the vicinity of the Charleston Bump. *Journal of Physical Oceanography*, **37**, 452–475.

Zhang, F., Snyder, C., and Rotunno, R., 2002, Mesoscale Predictability of the “Surprise” Snowstorm of 24-25 January 2000, *Monthly Weather Review*, **130**, 1617-1632.

Zhang, F., Snyder, C., and Rotunno, R., 2003, Effects of moist convection on mesoscale predictability. *Journal of Atmospheric Science*, **60**, 1173-1185.

Zhang, F., 2005, Dynamics and structure of mesoscale error covariance of a winter cyclone estimated through short-range ensemble forecasts. *Monthly Weather Review*, **133**, 2876-2893.

Zupanski, M., and Zupanski, D., Parrish, D. F., Rogers, E., and Dimego, G., 2002, Four-dimensional variational data assimilation for the blizzard of 2000. *Monthly Weather Review*, **130**, 1967-1988.

Fig. 1. The 2-m temperatures (dashed contours every 3°C), 10-m winds (barbs, kt), and sea-level pressure (solid contours every 3 hPa) from the NCEP North American Regional Reanalysis (NARR) valid (a) 0000 UTC 24 Jan, (b) 1200 UTC 24 Jan, (c) 0000 UTC 25 Jan, and (d) 0600 UTC 25 Jan.

Fig. 2. Sea surface temperatures for the CNTL (a) using NCEP 2.5° resolution data, and the EXP (b) using 1.1-km grid spacing data. Both the CNTL (a) and the EXP (b) simulation have been regridded to the 10-km model grid.

Fig. 3. Ship and buoy observations of SST valid 0000 UTC 23 Jan to 0000 UTC 25 2000, overlaid the post-cloud-filtered 1.1-km raw SST data valid 22 Jan 2000 (°C). The majority of these observations occurred within the front half of this time window, and are a combination of standard METAR Ship and Buoy, as well as additional observations from the National Data Buoy Center (NDBC). The circle marks a warm-core filament discussed throughout the text.

Fig. 4. Tracks for 24-25 January 2000 winter storm. The solid (green) line is the observed track (surface analysis performed by staff at the NWS WFO RAH), the dashed (red) line is the EXP simulation, and the dotted (blue) line is the CNTL simulation. Both simulations were initialized at 0000 UTC 24 Jan. Various positions of the storms are marked on the tracks with the corresponding times. Sea-level pressures are shown in the table inset for the respective times.

Fig. 5. Time series of sea-level pressure (mb) for the EXP simulation (solid red) and the CNTL simulation (dashed blue) from initialization time 0000 UTC 24 Jan (0 h) through 0000 UTC 26 Jan (48 h). Sea-level pressure observations (solid green) from METAR (land-based prior to 1500 UTC 24 Jan), and ship and buoy observations thereafter.

Fig. 6. The 2-m temperatures (shaded, K) and 10-m wind vectors (m s^{-1}) for the CNTL simulation (a) and the EXP simulation (b) valid 1200 UTC 24 Jan (12 h after initialization). The circles identify large regions of varying 2-m temperatures discussed in the text, and the arrow denotes circulation along a frontal boundary preceding the cyclone development.

Fig. 7. The 2-m temperatures (shaded, K) and 10-m wind vectors (m s^{-1}) for the CNTL simulation (a) and the EXP simulation (b) valid 0000 UTC 25 Jan (24 h after initialization). The circles identify large regions of varying 2-m temperatures discussed in the text. The arrow in (a) points to a region of convergence, while A (and B) point to the eastern side of the surface low (and the developing coastal front).

Fig. 8. The 10-m convergence (shaded, 10^{-4} s^{-1}) and σ-based level (approximately 700 hPa) of maximum divergence (dashed contours, 10^{-4} s^{-1}) valid 0000 UTC 25 Jan (24 h after initialization) for the CNTL simulation (a) and the EXP simulation (b).

Fig. 9. Cross section from 79°W to 72°W along 34.4°N showing convergence (solid contours, 10^{-4} s^{-1}), divergence (dashed contours, 10^{-4} s^{-1}), and vertical velocity (shaded, m s^{-1}) valid 0000 UTC 25 Jan (24 h after initialization) for the CNTL simulation (a) and the EXP simulation (b).

Fig. 10. The 10-m convergence (shaded, 10^{-4} s^{-1}) and σ-based level (approximately 700 hPa) of maximum divergence (dashed contours, 10^{-4} s^{-1}) valid 1200 UTC 25 Jan (36 h after initialization) for the CNTL simulation (a) and the EXP simulation (b). The cross sections from A to B are presented in Fig. 11.

Fig. 11. Cross sections from 35.25°N, 75°W to 38°N, 70°W for the CNTL and 36.25°N, 75°W to 39°N, 70°W for the EXP showing convergence (solid contours, 10^{-4} s^{-1}), divergence (dashed contours, 10^{-4} s^{-1}), and vertical velocity (shaded, m s^{-1}) valid 1200 UTC 25 Jan (36 h after initialization) for the CNTL simulation (a) and the EXP simulation (b).

Fig. 12. The surface-level sensible heat flux (W m^{-2}) and sea-level pressure (mb) valid 0000 UTC 25 Jan (24 h after initialization) for the CNTL simulation (a), the EXP simulation (b), and the EXP minus the CNTL (c). A is the region of similar sensible heat flux values. B and the black arrow represent locations of enhanced sensible heat flux seen in the EXP.

Fig. 13. The surface-level sensible heat flux (W m^{-2}) and sea-level pressure (mb) valid 1200 UTC 25 Jan (36 h after initialization) for the CNTL (a), EXP (b), and the EXP minus the CNTL (c). A is the region of similar sensible heat flux values, and B, C1, and C2 represent locations of enhanced sensible heat flux seen in the EXP.

Fig. 14. The 10-m wind field (shaded, m s^{-1}) and vectors for the CNTL (a) and the EXP (b) valid 0000 UTC 25 Jan (24 h after initialization). B (and C) represent different (and similar) 10-m wind velocities, and A is the developing coastal front in the EXP.

Fig. 15. The 10-m wind field (shaded, m s^{-1}) and vectors for the CNTL (a) and the EXP (b) valid 1200 UTC Jan 25 (36 h after initialization). A, and the region circled, represent regions of corresponding similar velocities, while B is a location with reduced 10-m winds discussed in the text.

Fig. 16. The 950-hPa vortex stretching (shaded, 10^{-7} s^{-2}), sea-level pressure (solid contours, hPa), and 10-m winds (barbs, kt) valid 0000 UTC 25 Jan (24 h after initialization) for the CNTL (a) and the EXP (b). A and B represent vortex stretching associated with the coastal frontogenesis discussed in the text.

Fig. 17. The simulated 48-h storm-total liquid-equivalent precipitation fields (mm) ending at 0000 UTC 26 Jan 2000 for the CNTL (a) and EXP (b). (c) The 48-h accumulated liquid-equivalent precipitation observations (mm) valid 0000 UTC 26 Jan 2000, which are derived from the 4-km multi-sensor precipitation analysis produced by NCEP/EMC using ASOS rain gauge data and hourly digital precipitation radar estimates.

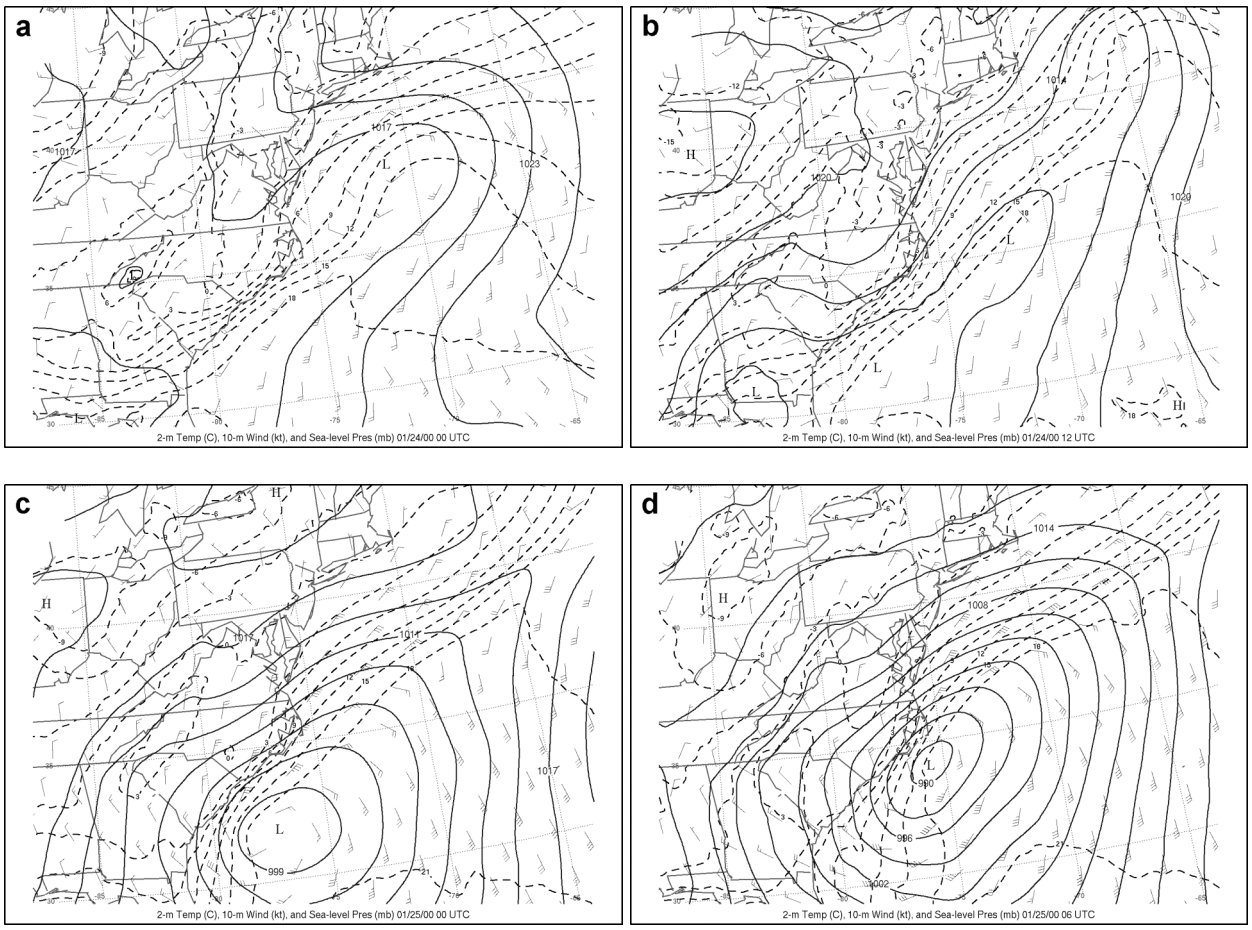

Fig. 1. The 2-m temperatures (dashed contours every 3°C), 10-m winds (barbs, kt), and sea-level pressure (solid contours every 3 hPa) from the NCEP North American Regional Reanalysis (NARR) valid (a) 0000 UTC 24 Jan, (b) 1200 UTC 24 Jan, (c) 0000 UTC 25 Jan, and (d) 0600 UTC 25 Jan.

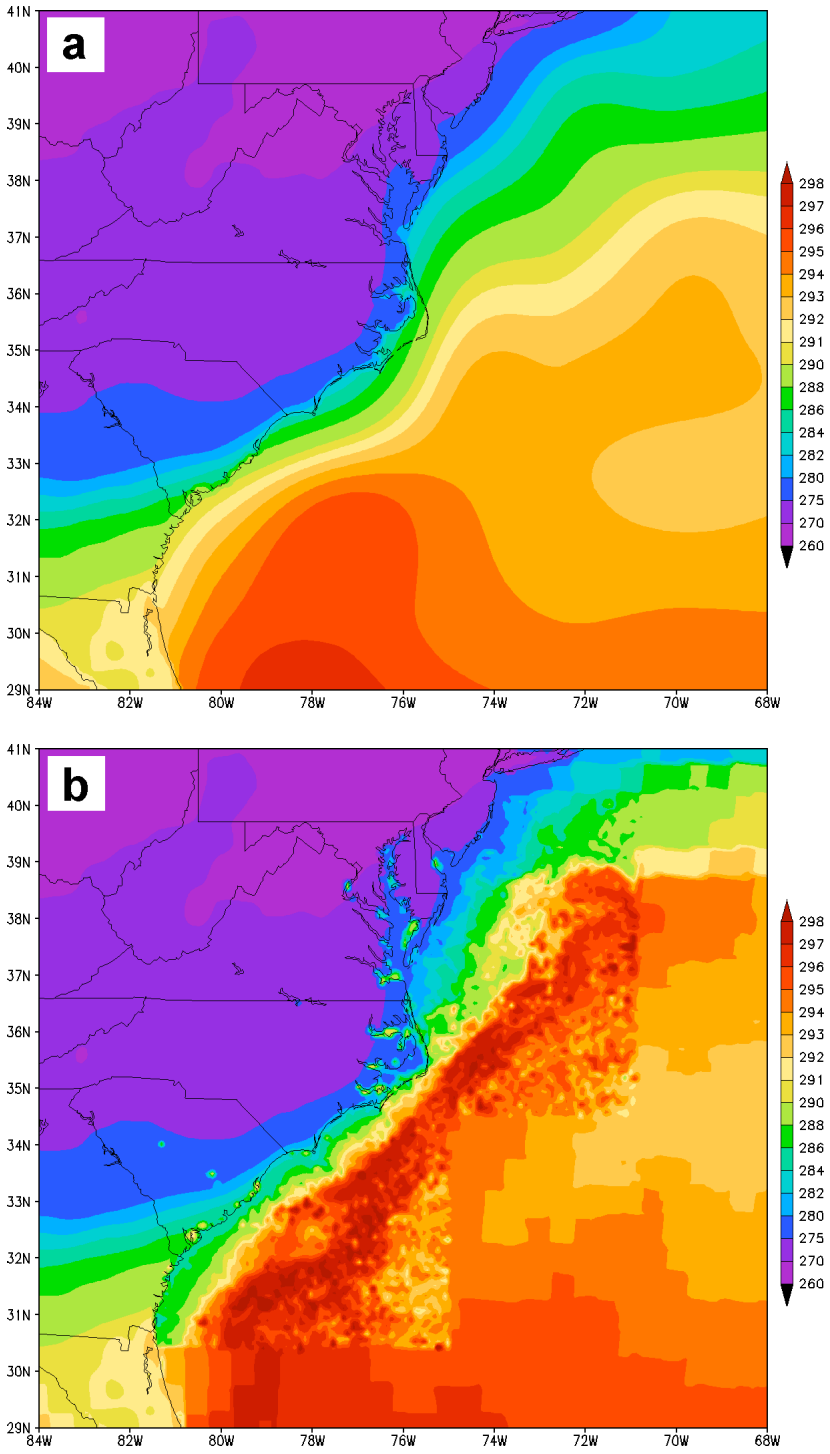

Fig. 2. Sea surface temperatures for the CNTL (a) using NCEP 2.5° resolution data, and the EXP (b) using 1.1-km grid spacing data. Both the CNTL (a) and the EXP (b) simulation have been regridded to the 10-km model grid.

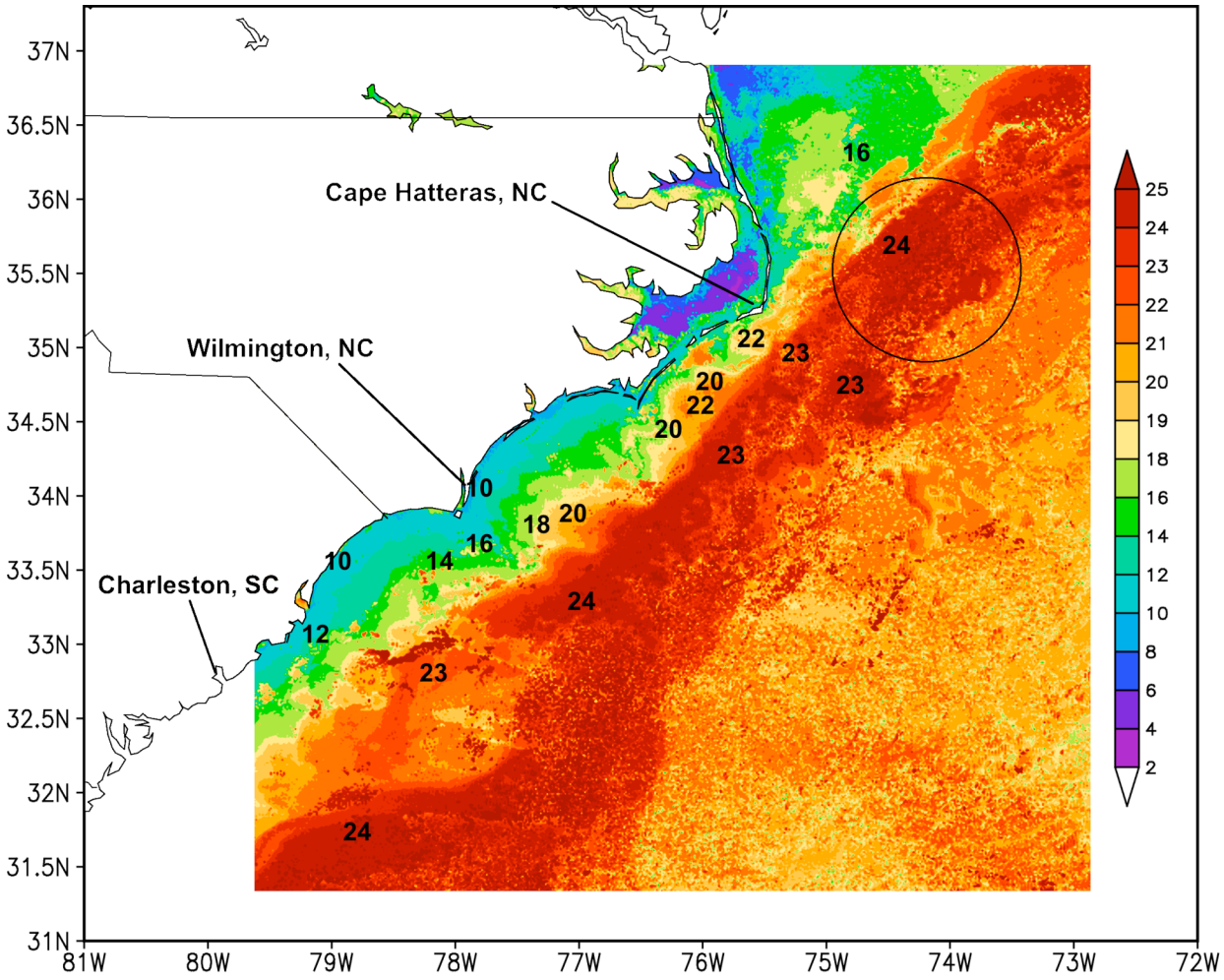

Fig. 3. Ship and buoy observations of SST valid 0000 UTC 23 Jan to 0000 UTC 25 2000, overlaid the post-cloud-filtered 1.1-km raw SST data valid 22 Jan 2000 (°C). The majority of these observations occurred within the front half of this time window, and are a combination of standard METAR Ship and Buoy, as well as additional observations from the National Data Buoy Center (NDBC). The circle marks a warm-core filament discussed throughout the text.

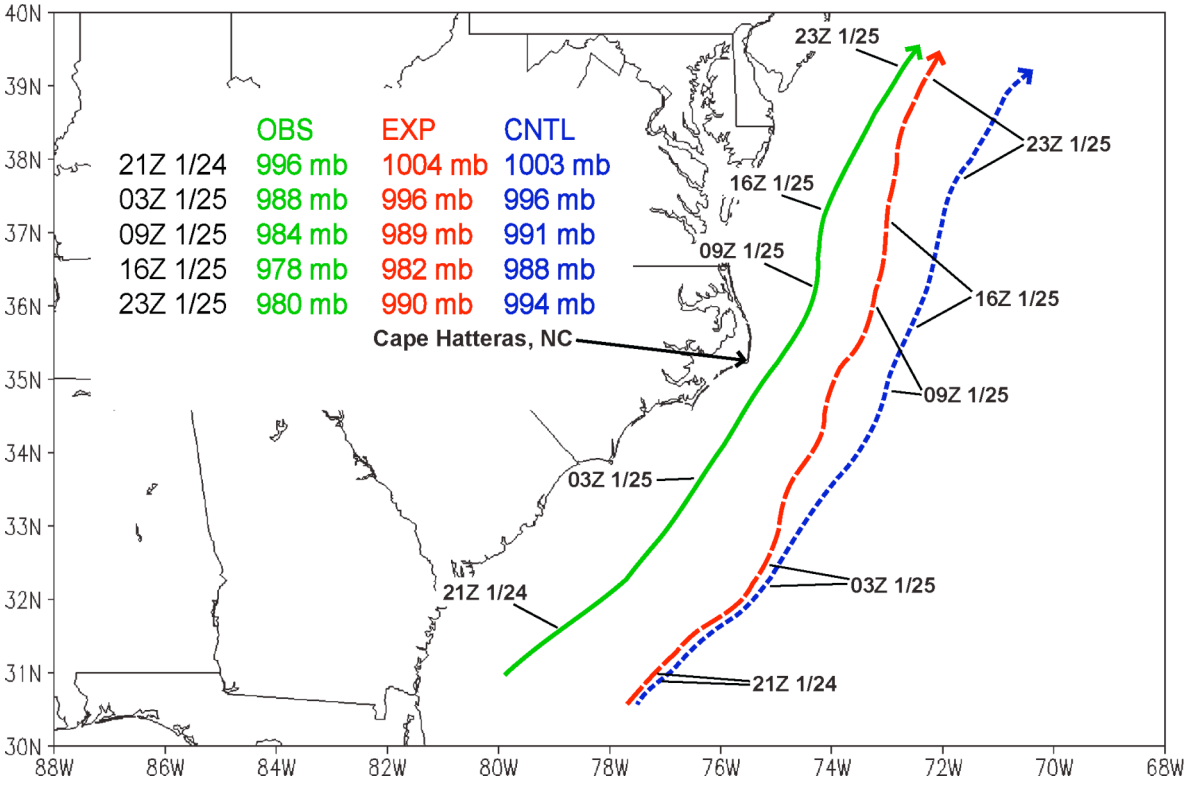

Fig. 4. Tracks for 24-25 January 2000 winter storm. The solid (green) line is the observed track (surface analysis performed by staff at the NWS WFO RAH), the dashed (red) line is the EXP simulation, and the dotted (blue) line is the CNTL simulation. Both simulations were initialized at 0000 UTC 24 Jan. Various positions of the storms are marked on the tracks with the corresponding times. Sea-level pressures are shown in the table inset for the respective times.

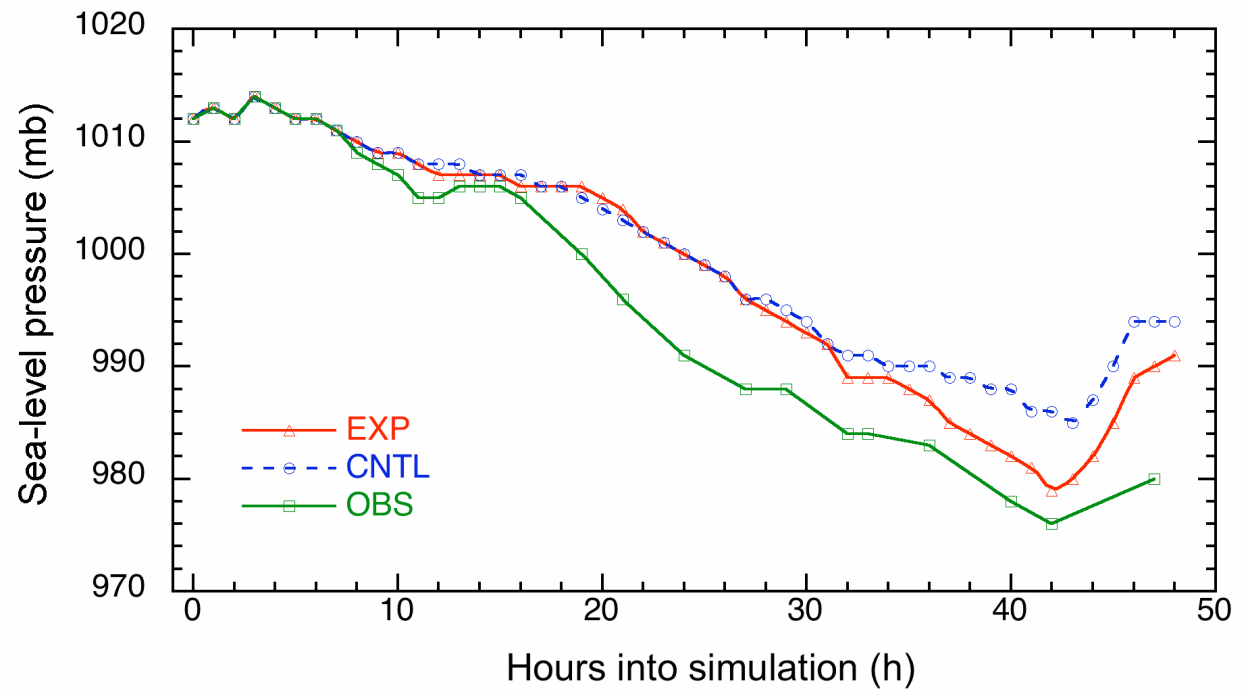

Fig. 5. Time series of sea-level pressure (mb) for the EXP simulation (solid red) and the CNTL simulation (dashed blue) from initialization time 0000 UTC 24 Jan (0 h) through 0000 UTC 26 Jan (48 h). Sea-level pressure observations (solid green) from METAR (land-based prior to 1500 UTC 24 Jan), and ship and buoy observations thereafter.

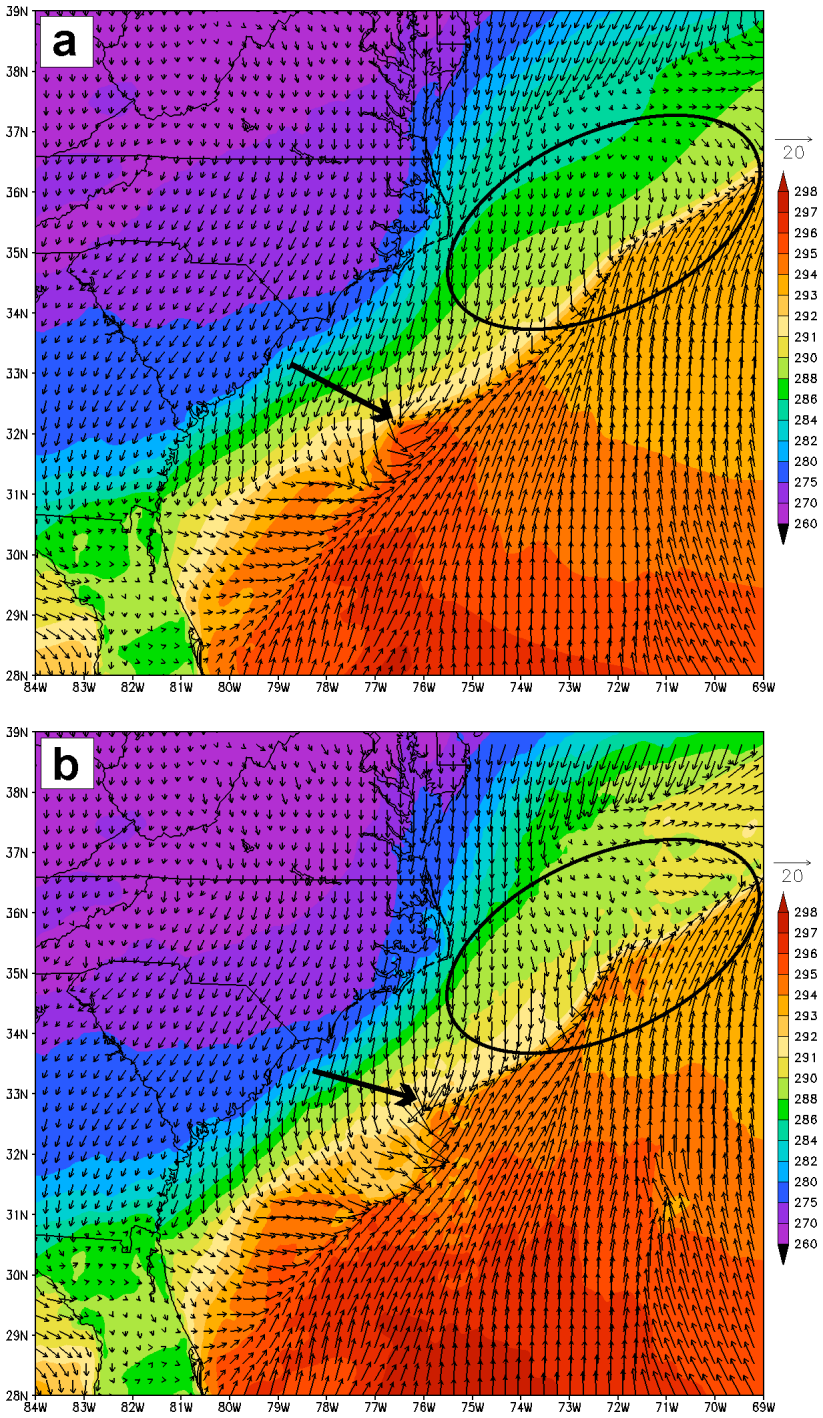

Fig. 6. The 2-m temperatures (shaded, K) and 10-m wind vectors (m s^{-1}) for the CNTL simulation (a) and the EXP simulation (b) valid 1200 UTC 24 Jan (12 h after initialization). The circles identify large regions of varying 2-m temperatures discussed in the text, and the arrow denotes circulation along a frontal boundary preceding the cyclone development.

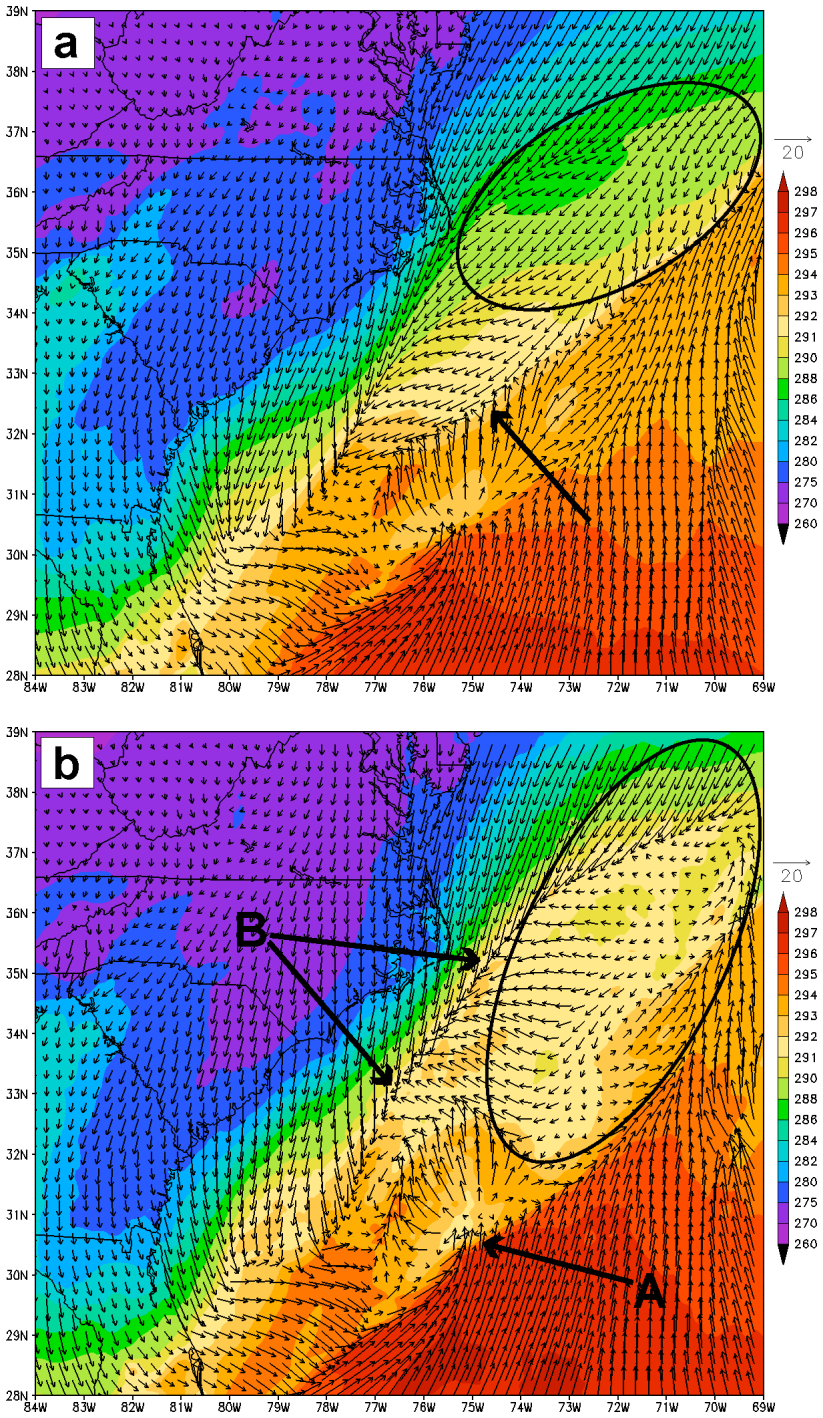

Fig. 7. The 2-m temperatures (shaded, K) and 10-m wind vectors (m s^{-1}) for the CNTL simulation (a) and the EXP simulation (b) valid 0000 UTC 25 Jan (24 h after initialization). The circles identify large regions of varying 2-m temperatures discussed in the text. The arrow in (a) points to a region of convergence, while A (and B) point to the eastern side of the surface low (and the developing coastal front).

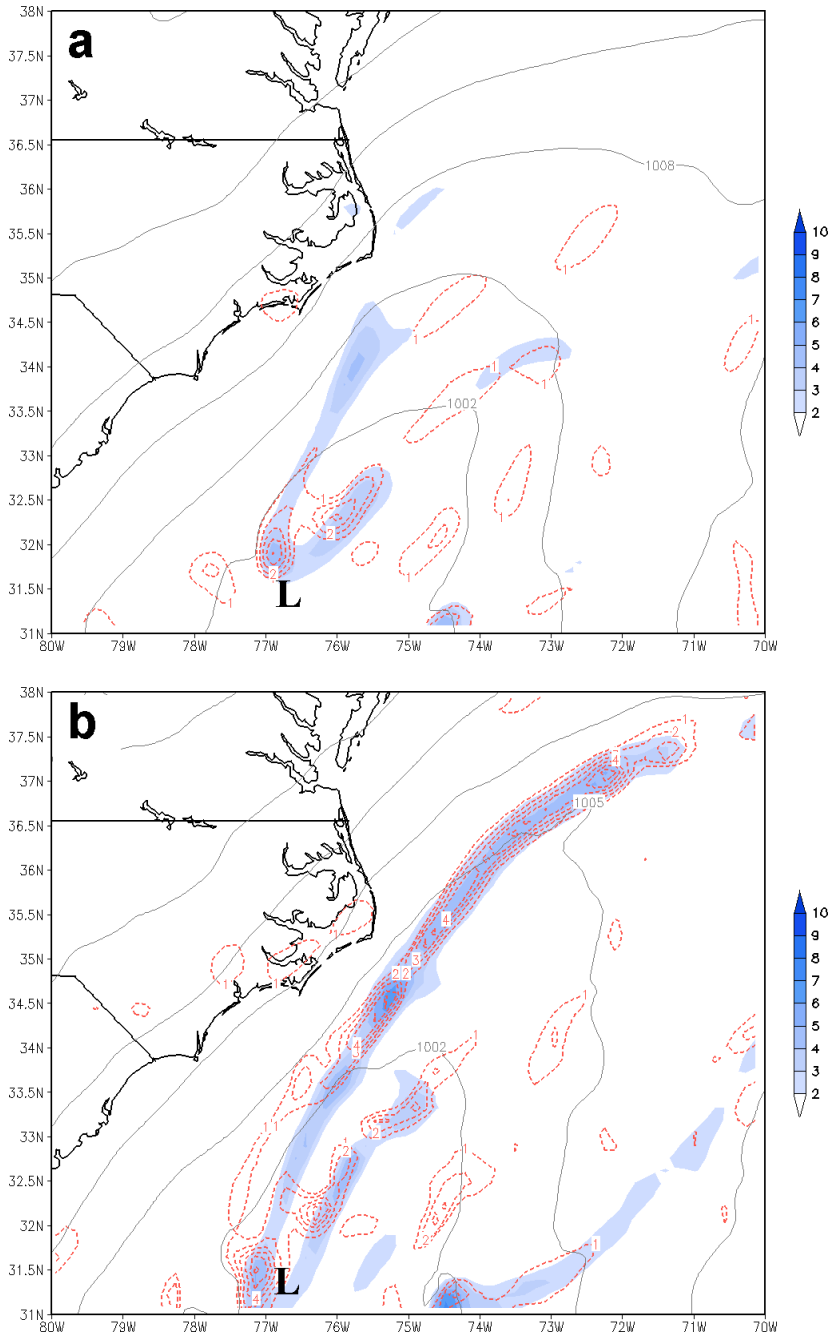

Fig. 8. The 10-m convergence (shaded, 10^{-4} s^{-1}) and σ-based level (approximately 700 hPa) of maximum divergence (dashed contours, 10^{-4} s^{-1}) valid 0000 UTC 25 Jan (24 h after initialization) for the CNTL simulation (a) and the EXP simulation (b).

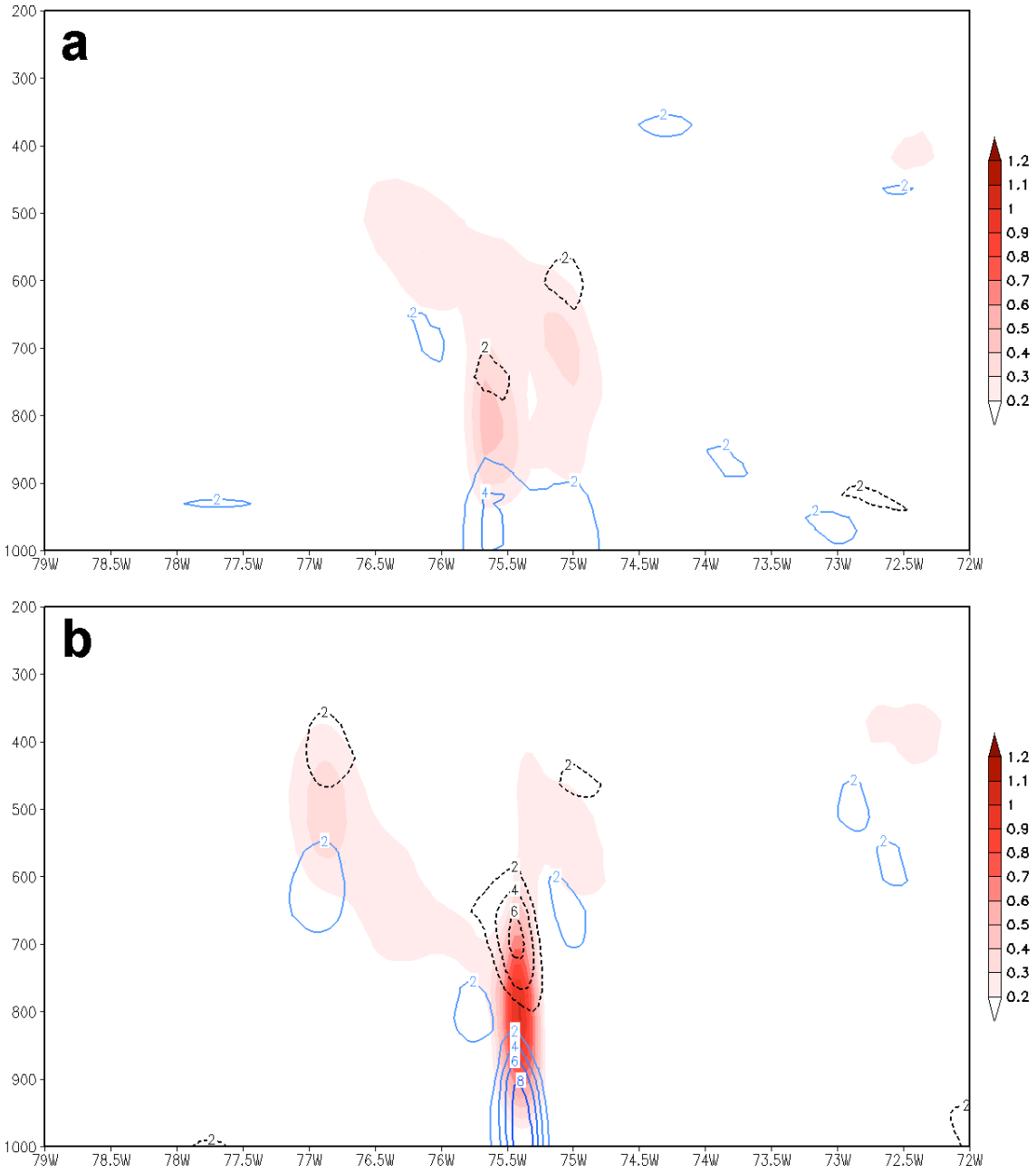

Fig. 9. Cross section from 79°W to 72°W along 34.4°N showing convergence (solid contours, 10^{-4} s^{-1}), divergence (dashed contours, 10^{-4} s^{-1}), and vertical velocity (shaded, m s^{-1}) valid 0000 UTC 25 Jan (24 h after initialization) for the CNTL simulation (a) and the EXP simulation (b).

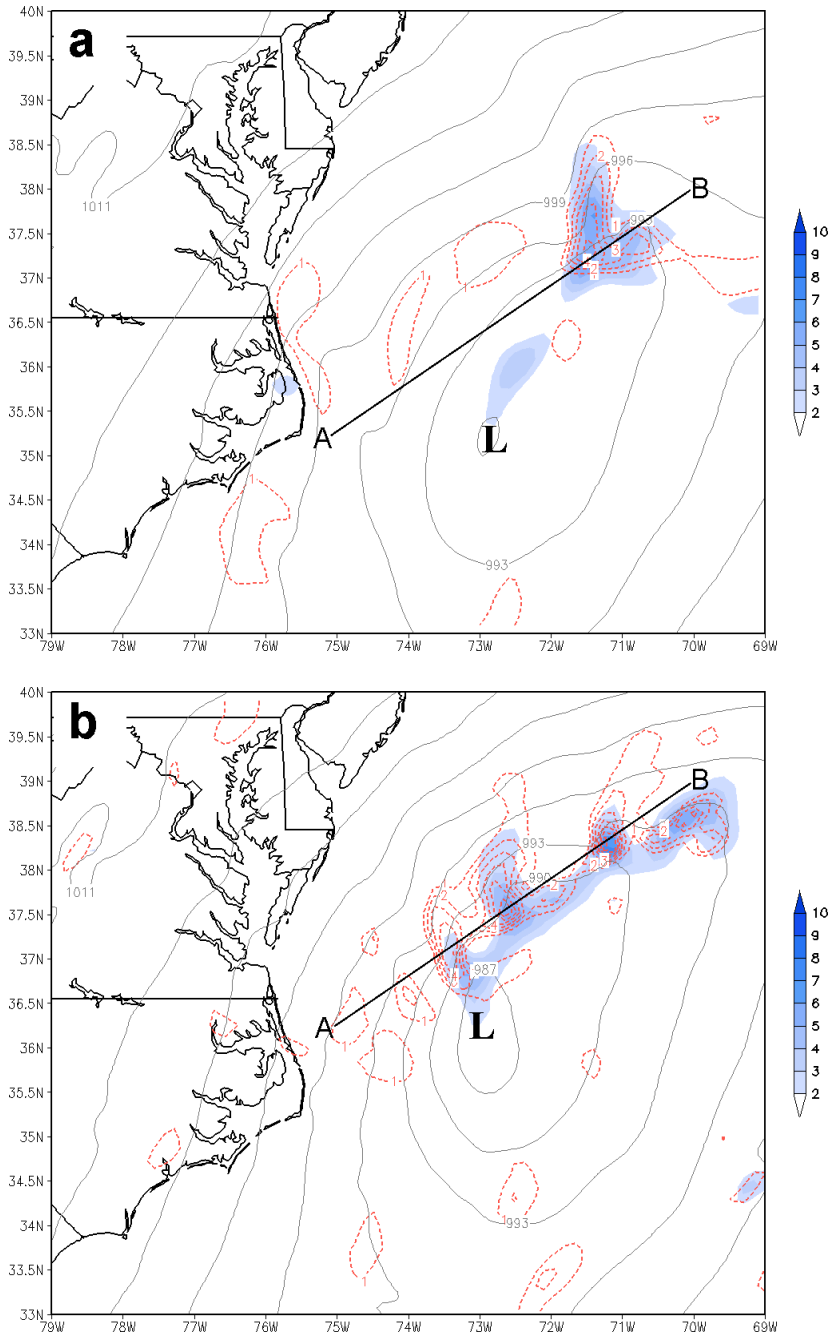

Fig. 10. The 10-m convergence (shaded, 10^{-4} s^{-1}) and σ-based level (approximately 700 hPa) of maximum divergence (dashed contours, 10^{-4} s^{-1}) valid 1200 UTC 25 Jan (36 h after initialization) for the CNTL simulation (a) and the EXP simulation (b). The cross sections from A to B are presented in Fig. 11.

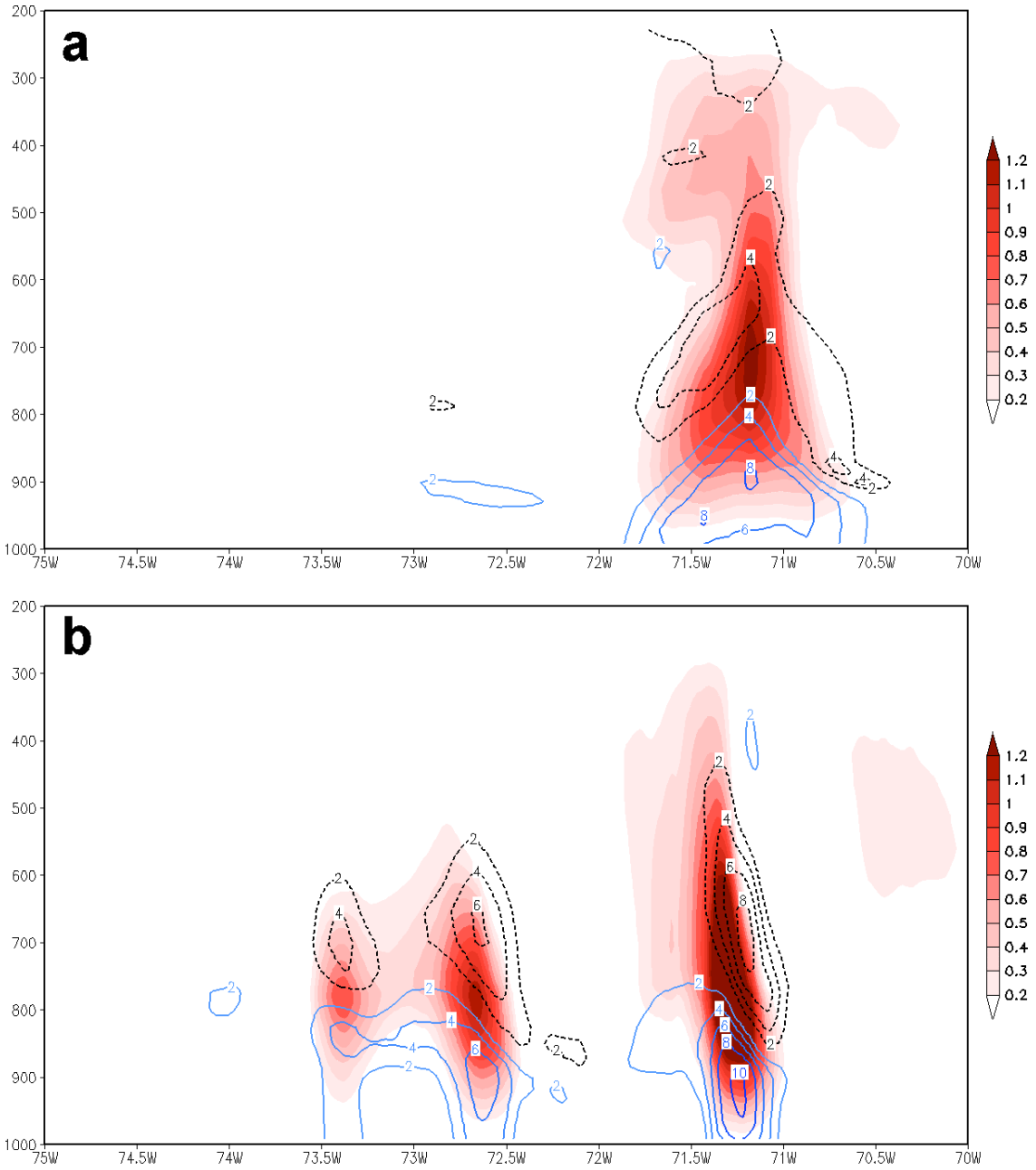

Fig. 11. Cross sections from 35.25°N, 75°W to 38°N, 70°W for the CNTL and 36.25°N, 75°W to 39°N, 70°W for the EXP showing convergence (solid contours, 10^{-4} s^{-1}), divergence (dashed contours, 10^{-4} s^{-1}), and vertical velocity (shaded, m s^{-1}) valid 1200 UTC 25 Jan (36 h after initialization) for the CNTL simulation (a) and the EXP simulation (b).

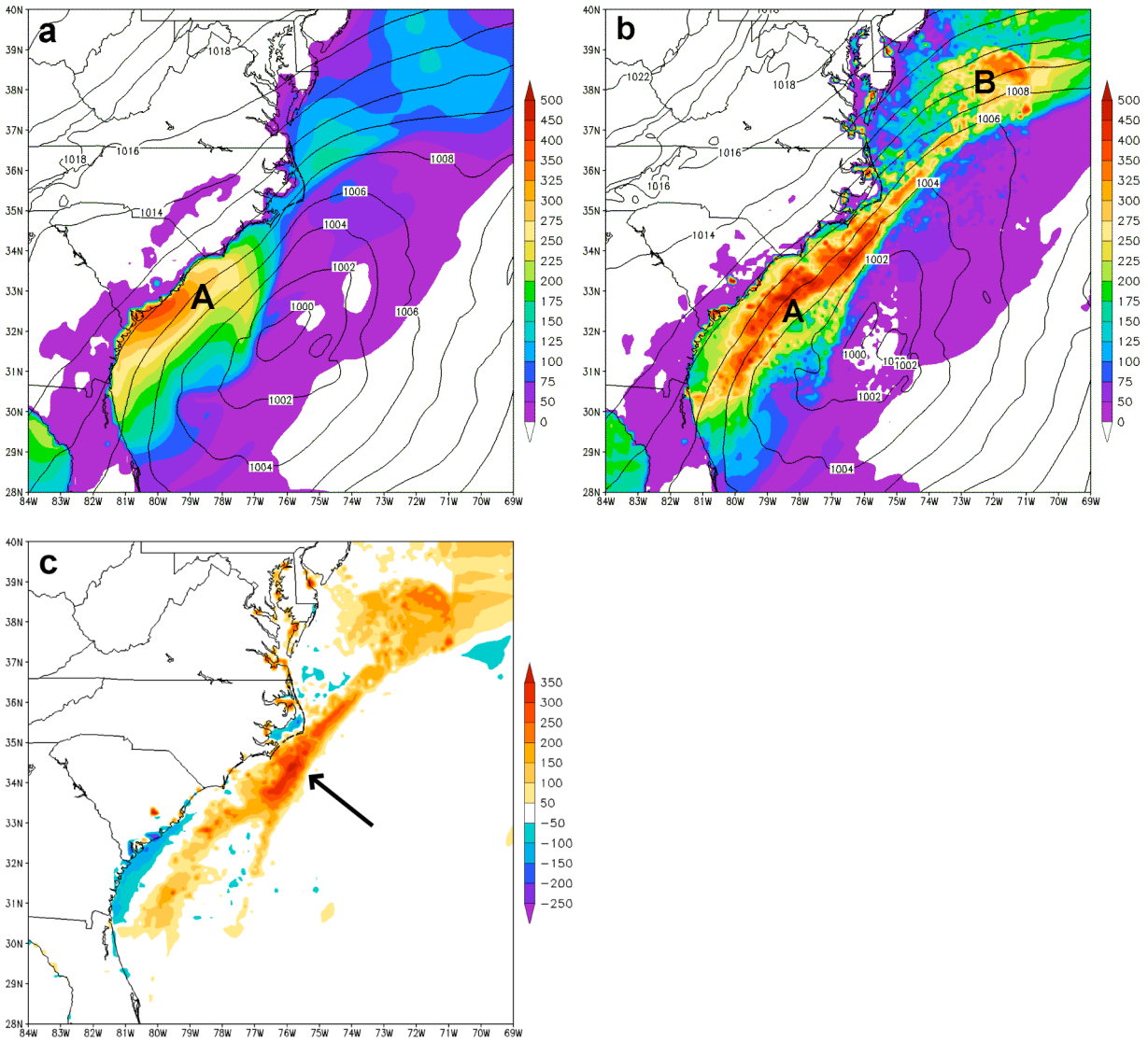

Fig. 12. The surface-level sensible heat flux (W m^{-2}) and sea-level pressure (mb) valid 0000 UTC 25 Jan (24 h after initialization) for the CNTL simulation (a), the EXP simulation (b), and the EXP minus the CNTL (c). A is the region of similar sensible heat flux values. B and the black arrow represent locations of enhanced sensible heat flux seen in the EXP.

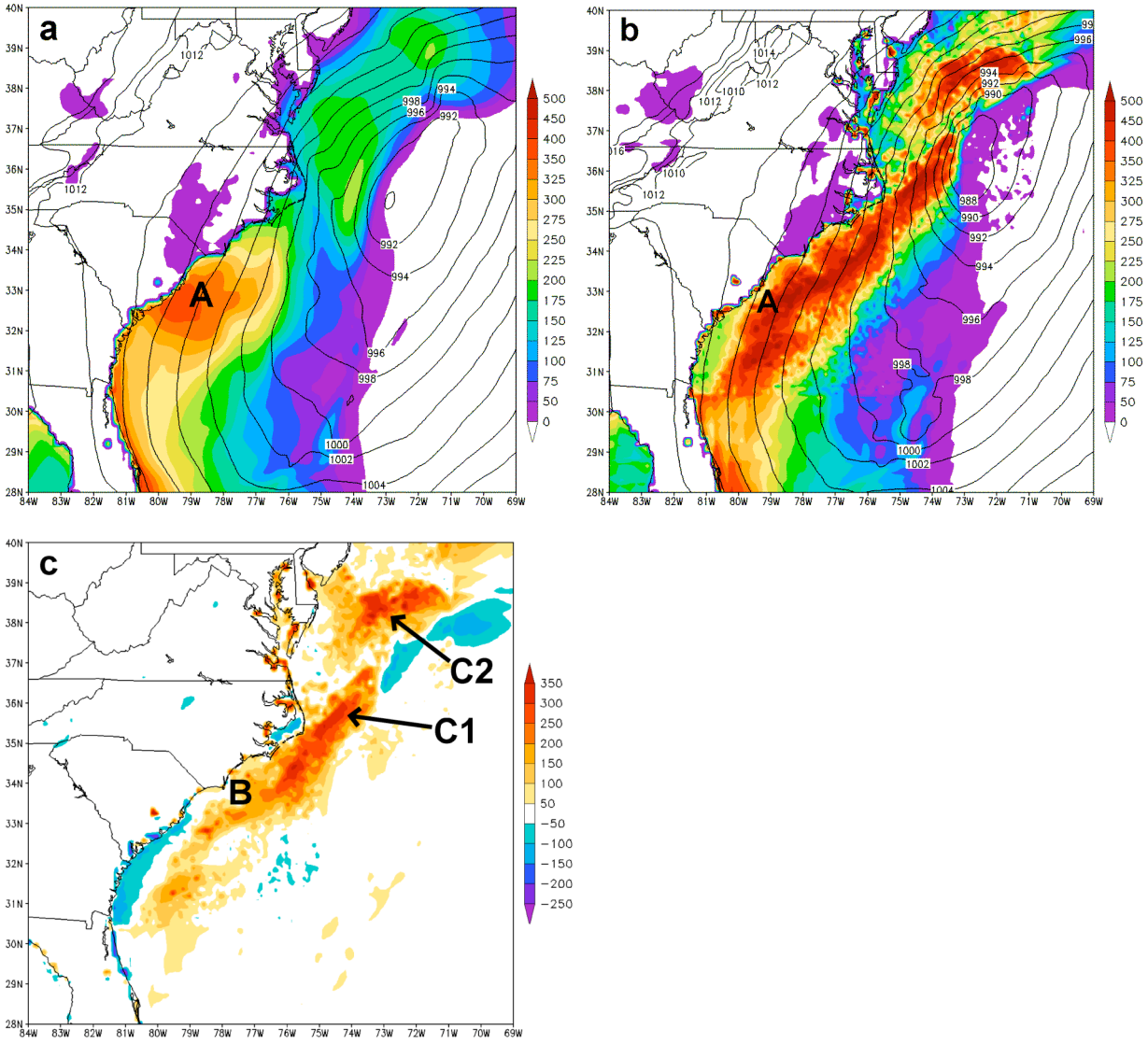

Fig. 13. The surface-level sensible heat flux (W m^{-2}) and sea-level pressure (mb) valid 1200 UTC 25 Jan (36 h after initialization) for the CNTL (a), EXP (b), and the EXP minus the CNTL (c). A is the region of similar sensible heat flux values, and B, C1, and C2 represent locations of enhanced sensible heat flux seen in the EXP.

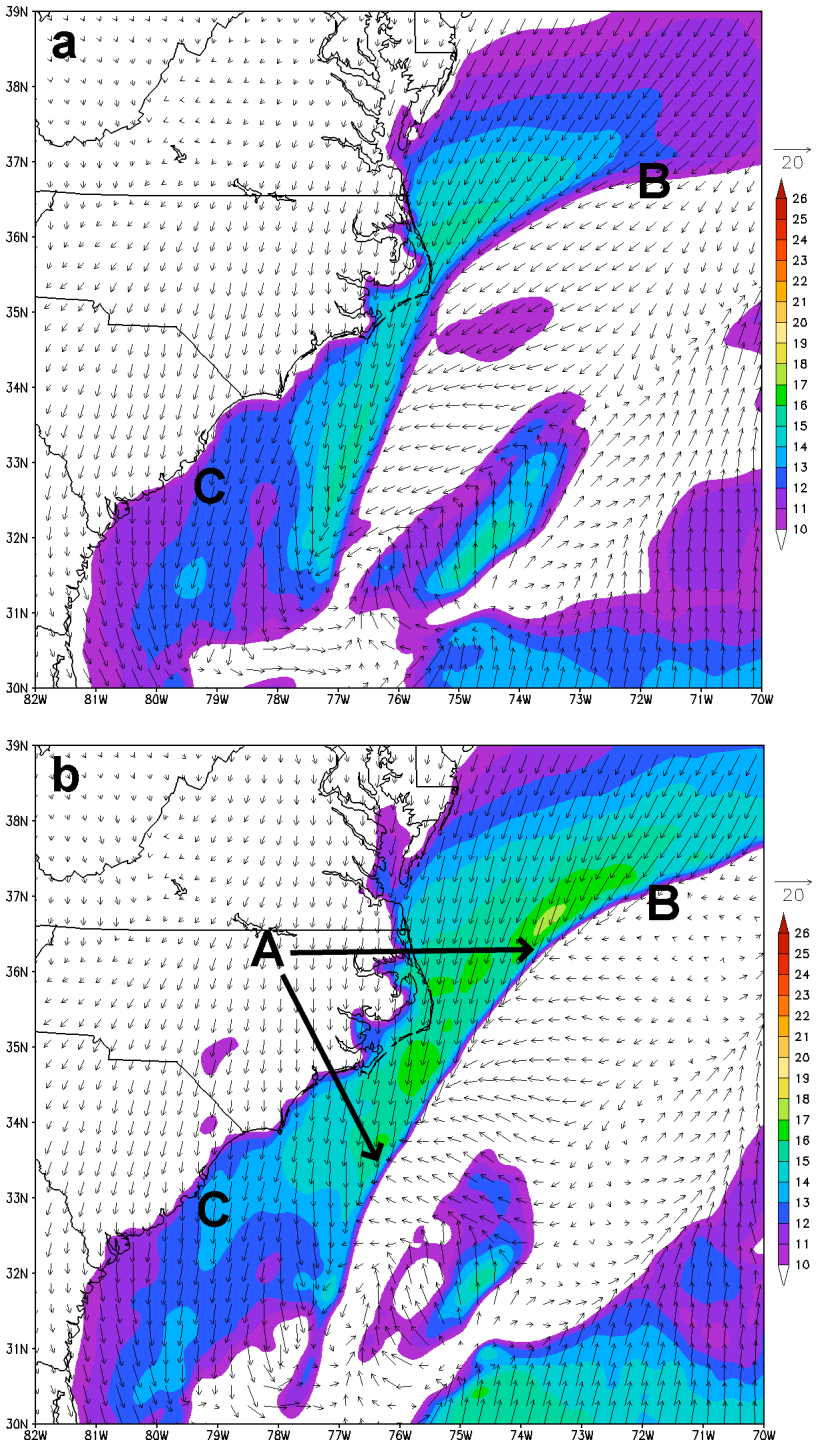

Fig. 14. The 10-m wind field (shaded, m s^{-1}) and vectors for the CNTL (a) and the EXP (b) valid 0000 UTC 25 Jan (24 h after initialization). B (and C) represent different (and similar) 10-m wind velocities, and A is the developing coastal front in the EXP.

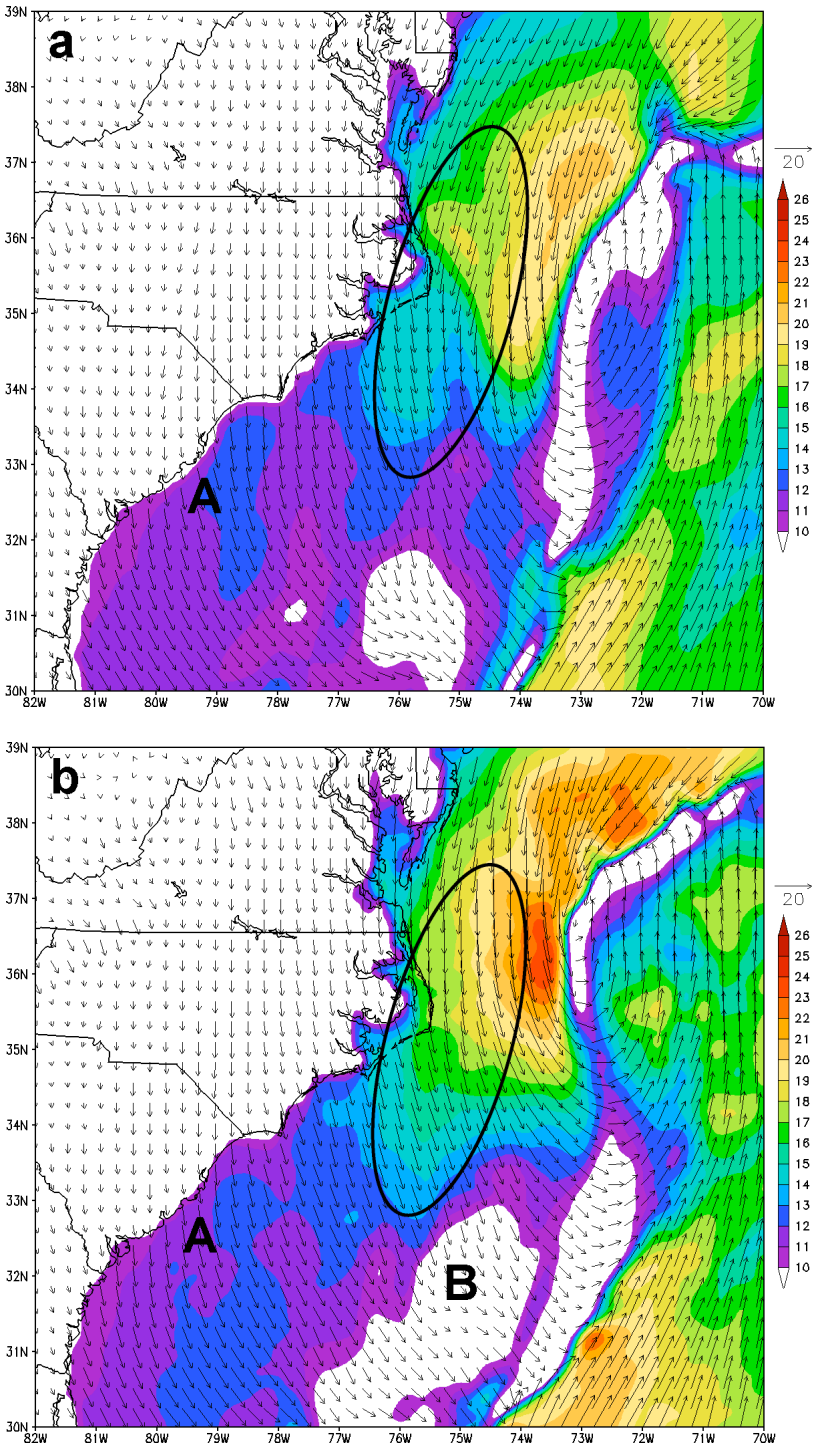

Fig. 15. The 10-m wind field (shaded, m s^{-1}) and vectors for the CNTL (a) and the EXP (b) valid 1200 UTC Jan 25 (36 h after initialization). A, and the region circled, represent regions of corresponding similar velocities, while B is a location with reduced 10-m winds discussed in the text.

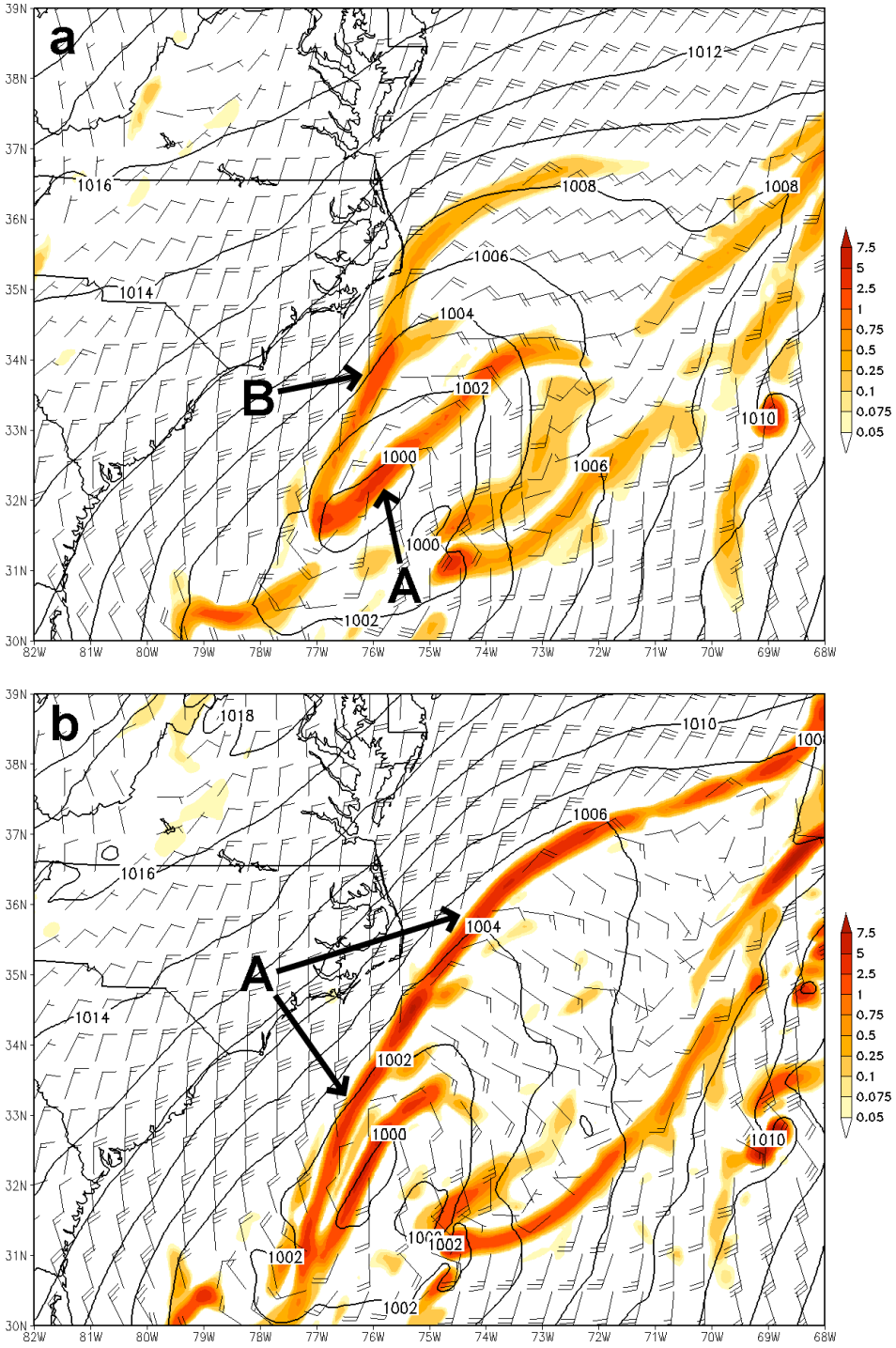

Fig. 16. The 950-hPa vortex stretching (shaded, 10^{-7} s^{-2}), sea-level pressure (solid contours, hPa), and 10-m winds (barbs, kt) valid 0000 UTC 25 Jan (24 h after initialization) for the CNTL (a) and the EXP (b). A and B represent vortex stretching associated with the coastal frontogenesis discussed in the text.

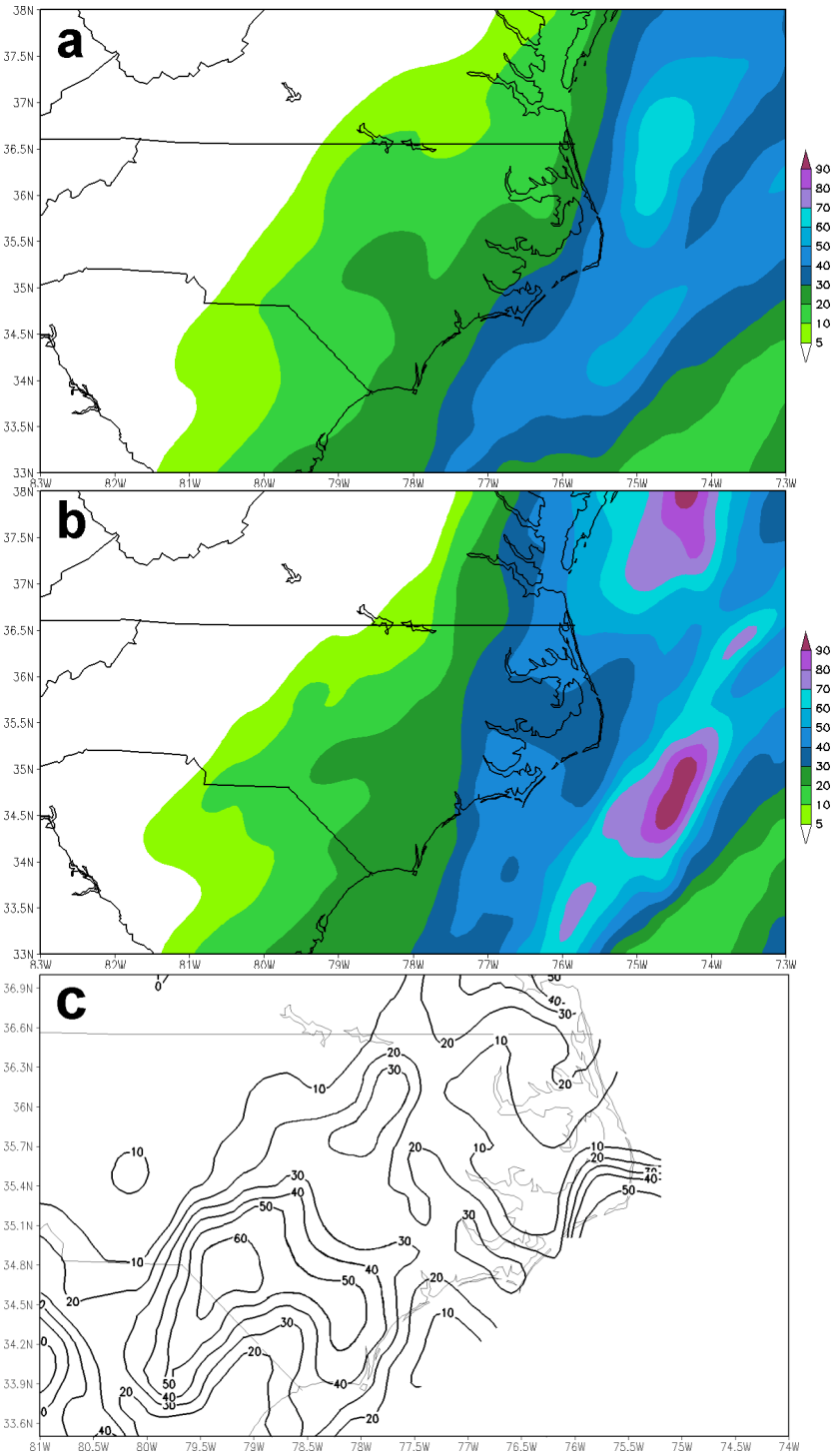

Fig. 17. The simulated 48-h storm-total liquid-equivalent precipitation fields (mm) ending at 0000 UTC 26 Jan 2000 for the CNTL (a) and EXP (b). (c) The 48-h accumulated liquid-equivalent precipitation observations (mm) valid 0000 UTC 26 Jan 2000, which are derived from the 4-km multi-sensor precipitation analysis produced by NCEP/EMC using ASOS rain gauge data and hourly digital precipitation radar estimates.